Assessment of a High-Order MUSCL Method for Rotor Flows

A. Jimenez-Garcia[a], G. N. Barakos[b]
CFD Laboratory, School of Engineering,
University of Glasgow, G12 8QQ Glasgow, UK

This work presents the implementation of a high-order, finite-volume scheme suitable for rotor flows. The formulation is based on the variable extrapolation MUSCL-scheme, where high-order spatial accuracy (up to 4th-order) is achieved using correction terms obtained through successive differentiation. A variety of results are presented, including two-and three-dimensional test cases. Results with the proposed scheme, showed better wake and higher resolution of vortical structures compared with the standard MUSCL, even when coarse meshes were employed. The method was also demonstrated for three-dimensional unsteady flows using overset and moving grids for the UH-60A rotor in forward flight and the ERICA tiltrotor in aeroplane mode. For medium grids, the present method adds reasonable CPU and memory overheads and offers good accuracy on relatively coarse grids.

[a] PhD Candidate, CFD Laboratory, School of Engineering, Email: a.jimenez-garcia.1@research.gla.ac.uk
[b] Professor, MAIAA, MRAeS, CFD Laboratory, School of Engineering, Email: George.Barakos@glasgow.ac.uk

I. Introduction

In recent years, significant progress has been made in accurately predicting rotorcraft flows using Computational Fluid Dynamics (CFD) [1]. Nevertheless, computational aeroacoustics, and the need to resolve the wake far from rotor, call for high resolution methods, if results are to be obtained on grids of reasonable density [1–3]. In addition, since first and second-order methods are dissipative, high-order methods are needed to accurately predict vortex dominated flows (e.g. vortex wake of a helicopter rotor in hover [4]). However, high-order schemes are less robust and slower to converge to steady-state solutions than low-order methods, and present higher memory requirements especially when implicit time stepping techniques are required.

A numerical method is K-order accurate if the solution error e is proportional to the mesh size h raised to a power K. If K is greater or equal than three, the method is considered "high-order". The reason of this criterion ($K \geq 3$) is due to the fact that most CFD solvers used in the aerospace community are second-order accurate. Given the same CPU time, high-order methods achieve high level of accuracy on coarse grids than low-order methods, so they are more efficient.

Several types of high-order methods have been developed in the past three decades to cope with a wide range of problems. Spectral methods firstly introduced by Orszag *et al.* [5] and first-order schemes (Godunov's scheme [6]) represent the most and least accurate methods, respectively. A first classification covers high-order schemes developed either for structured [7, 8] or unstructured meshes [9–12]. The formulation of those methods in Finite-Difference (FD) [13, 14] or Finite-Volume (FV) [15, 16] frameworks is also a means of classification. A more complete classification is given by Ekaterinaris [17] in his review paper.

Numerous studies in high-order methods have been formulated in the FD framework [13] and is well known that FD schemes have advantages in developing high-order spatial discretisation methods. However, they can only be applied on smooth, structured, and curvilinear meshes. In this regard, Tam *et al.* [13] developed a high-order Dispersion-Relation-Preserving (DRP) finite difference scheme, where the high-order derivatives were computed in the wave number and frequency space (using Fourier transforms) which led to preserve the dispersion relation of the scheme. Visbal *et al.* [14] applied a high-order methods (up to 6th-order accurate) on a structured curvilinear mesh using implicit and compact finite-difference schemes. The method was observed to be robust through the use of a spatial filtering strategy (low-pass Pade-type non-dispersive) that smoothed the solution.

By contrast, FV formulations are the most popular choice for the discretisation of the fluid flow equations. Despite these methods being robust, they are typically restricted to second-order accuracy in space [18].

In gas dynamics, it is common to find problems that involve shocks and other discontinuities or high gradient regions in the solution, making it difficult to develop stable and robust high-order methods. To address this issue, Essentially Non-Oscillatory (ENO) [19–21] and Weighted

Essentially Non-Oscillatory (WENO) [8] schemes were designed and applied to complex flows. In 1994, the first WENO scheme was designed by Liu *et al.* [8] and was third-order accurate in a finite-volume framework. Two years later, Jiang *et al.* [22] extended the WENO schemes to multi-space dimensions using third and fifth-order finite differences, whilst Balsara *et al.* [23] developed higher-order finite difference schemes (up to 11th-order accurate). A substantial effort was also made to construct compact central WENO schemes [24, 25]. Along with the WENO scheme, a Compact-Reconstruction Weighted Essentially Non-Oscillatory Scheme (CRWENO) was introduced by Ghosh [26] (up to 5th-order accurate) using the finite-volume method. A more detailed review of ENO and WENO schemes can be found in the work of Shu [27].

This paper demonstrates a high-order method (up to 4th-order), which is achieved using high-order correction terms through successive differentiation [11, 12]. The method can be implemented as a correction to existing MUSCL schemes and offers good accuracy with very easy implementation in existing codes. Unlike ENO and WENO schemes [28–30], MUSCL schemes are easier to code and represent a good compromise between level of accuracy and CPU and memory overheads for rotorcraft applications.

The structure of this paper is as follows. First, a high-order scheme using a successive differentiation approach is derived for one-dimensional (1D) problems, where spectral resolution properties (dissipation and dispersion errors) are also shown. Then, results obtained with the new scheme for a wide variety of test cases are presented. The application of the scheme to Euler's equations covers the first part, where a convection of an isentropic vortex and the aerodynamic interaction between a vortex and a NACA-0012 aerofoil (blade-vortex interaction) are studied. The new methodology is extended and applied to steady, transonic, turbulent flow, where the capability of the scheme in preserving accuracy under non-smooth solution is investigated using the RAE2822 transonic aerofoil. Moreover, three-dimensional steady flows around the 7AD and S-76 rotor, the JORP propeller, and the XV-15 tiltrotor blades are put forward, as a means of comparing the resolution of near-blade and wake flow features with standard MUSCL results with the same CFD code. Finally, the capability of the present method in preserving the wake structure for complex unsteady flows such the UH-60A rotor in forward flight and the ERICA tiltrotor in aeroplane mode is also showcased.

This high-order method (up to 4th-order) was presented by Yang *et al.* [11, 12] and implemented into an unstructured CFD solver. To the author's knowledge, this is the first time that this kind of scheme is implemented in a structured finite-volume CFD method and demonstrated for rotor flows. Moreover, the application of the scheme to three-dimensional steady and unsteady flows around complex geometries with the use of the chimera technique is also novel.

The Helicopter Multi-Block (HMB) code will be used to demonstrate the scheme [31–34]. This is a well-validated tool used by academia [4] and industry [35] for rotorcraft CFD.

II. High-order formulation

This section describes the formulation of the high-order correction terms. This formulation was firstly proposed by Burg [36] for unstructured finite-volume codes, where a third-order spatial accuracy was achieved for two-and three-dimensional problems. Yang *et al.* [11, 12] extended the scheme to fourth-order spacial accuracy. The scheme resembles the MUSCL-schemes [37] (Monotonic Upstream-centered Scheme for Conservation Laws) and used here to discretised the convective part of the Navier–Stokes equations. It represents a one-parameter family of equations, where a third-order spatial accuracy can be achieved. For 1-dimensional problems and on uniform grids (see Figure 1), the extrapolation of the flow variables to both sides of the cell-face located at $j+1/2$ for a MUSCL-scheme is given:

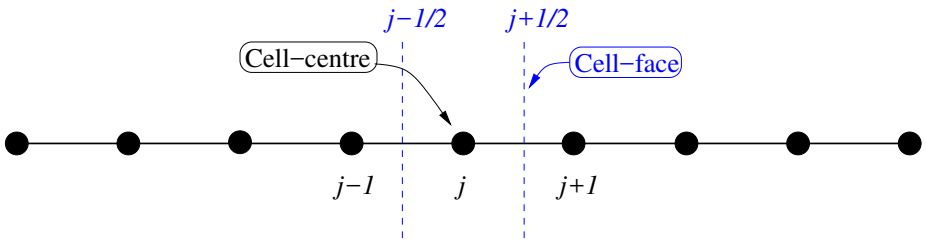

Fig. 1: Illustration of the domain discretisation.

$$\mathbf{F}^{\mathrm{L}}_{j+1/2} \;=\; \mathbf{F}_j + \left[\frac{k_1}{2}(\mathbf{F}_{j+1}-\mathbf{F}_j) + (1-k_1)\vec{\nabla}\mathbf{F}_j \bullet \vec{\mathbf{r}}_{f_j}\right] \tag{1}$$

$$\mathbf{F}^{\mathrm{R}}_{j+1/2} \;=\; \mathbf{F}_{j+1} - \left[\frac{k_1}{2}(\mathbf{F}_{j+1}-\mathbf{F}_j) + (1-k_1)\vec{\nabla}\mathbf{F}_{j+1} \bullet \vec{\mathbf{r}}_{f_{j+1}}\right] \tag{2}$$

In Eqns. 1 and 2, the vectors $\vec{\mathbf{r}}_{f_j}$ and $\vec{\mathbf{r}}_{f_{j+1}}$ represent the distances between the cell-face $j+1/2$ and the cell-centre volumes j, and $j+1$, respectively. To reconstruct the gradient $\vec{\nabla}\mathbf{F}_j$ and $\vec{\nabla}\mathbf{F}_{j+1}$ at cell-centre volumes j and $j+1$, either the Green-Gauss or the Least-Squares approaches can be used. By setting $k_1 = 0$, a 2nd-order upwind scheme is obtained. If $k_1 = 1/3$, a third order, upwind biased scheme is derived [38]. If k_1 is set to 1, a 2nd-order central difference scheme is obtained. It is clear that the present MUSCL-schemes are limited to third-order accurate.

Following Yang *et al.* [11], the proposed 4th-order structured MUSCL scheme is written in a similar fashion, where the extrapolation to both sides of the face located at $j+1/2$ is given as:

$$\begin{aligned}\mathbf{F}^{\mathrm{L}}_{j+1/2} \;=\; & \overbrace{\mathbf{F}_j + \frac{k_1}{2}(\mathbf{F}_{j+1}-\mathbf{F}_j) + (1-k_1)\vec{\nabla}\mathbf{F}_j \bullet \vec{\mathbf{r}}_{f_j}}^{\text{Standard MUSCL for the left state}} \\ & \underbrace{+\frac{1}{2}\left[\frac{k_2}{2}\left(\vec{\nabla}\mathbf{F}_{j+1}\bullet\vec{\mathbf{r}}_{f_j} - \vec{\nabla}\mathbf{F}_j\bullet\vec{\mathbf{r}}_{f_j}\right) + (1-k_2)\vec{\nabla}\left(\vec{\nabla}\mathbf{F}_j\bullet\vec{\mathbf{r}}_{f_j}\right)\bullet\vec{\mathbf{r}}_{f_j}\right]}_{\text{High-order corrections for the left state}}\end{aligned} \tag{3}$$

$$\mathbf{F}^{\mathrm{R}}_{j+1/2} = \overbrace{\mathbf{F}_{j+1} - \frac{k_1}{2}(\mathbf{F}_{j+1} - \mathbf{F}_j) - (1-k_1)\vec{\nabla}\mathbf{F}_{j+1} \bullet \vec{\mathbf{r}}_{f_{j+1}}}^{\text{Standard MUSCL for the right state}} \underbrace{+\frac{1}{2}\left[\frac{k_2}{2}\left(\vec{\nabla}\mathbf{F}_{j+1} \bullet \vec{\mathbf{r}}_{f_{j+1}} - \vec{\nabla}\mathbf{F}_{j} \bullet \vec{\mathbf{r}}_{f_{j+1}}\right) + (1-k_2)\vec{\nabla}\left(\vec{\nabla}\mathbf{F}_{j+1} \bullet \vec{\mathbf{r}}_{f_{j+1}}\right) \bullet \vec{\mathbf{r}}_{f_{j+1}}\right]}_{\text{High-order corrections for the right state}} \tag{4}$$

As can be observed, this new variable extrapolation formulation represents a two-parameter family (k_1 and k_2), and is equivalent to the standard MUSCL-scheme under certain values of k_1 and k_2. As shown in Eqns. 3 and 4, the high-order correction terms have been developed using a Taylor series expansion about the centre of the face $j+1/2$. The terms require knowledge of the second derivatives $\vec{\nabla}\left(\vec{\nabla}\mathbf{F}_j \bullet \vec{\mathbf{r}}_{f_j}\right)$ and $\vec{\nabla}\left(\vec{\nabla}\mathbf{F}_{j+1} \bullet \vec{\mathbf{r}}_{f_{j+1}}\right)$. Once the first derivatives are computed, the second derivatives can be estimated by successive application of the Green-Gauss or the Least Squares methods to the first derivatives.

Regarding the standard HMB solver, gradients $\vec{\nabla}\mathbf{F}_j$ and $\vec{\nabla}\mathbf{F}_{j+1}$ at cell-centre volumes j and $j+1$ are computed using a second-order finite difference approximation:

$$\vec{\nabla}\mathbf{F}_j \bullet \vec{\mathbf{r}}_{f_j} = \frac{1}{4}\Big(\mathbf{F}_{j+1} - \mathbf{F}_{j-1}\Big). \tag{5}$$

$$\vec{\nabla}\mathbf{F}_{j+1} \bullet \vec{\mathbf{r}}_{f_{j+1}} = \frac{1}{4}\Big(\mathbf{F}_{j+2} - \mathbf{F}_{j}\Big). \tag{6}$$

This formulation is less expensive than Green-Gauss or Least Squares methods, and it does not require exchanging data for parallel execution. So, this presents a compromise between accuracy and computational time. However, this approximation can not be used when high-order schemes are employed as will be discussed in the next paragraph.

A. Green-Gauss Formulation

As discussed earlier, to reconstruct the gradient $\vec{\nabla}\mathbf{F}_j$ and $\vec{\nabla}\mathbf{F}_{j+1}$ at cell-centre volumes j and $j+1$, either the Green-Gauss or the Least-Squares approaches can be considered. It is well known, that the Least-Square approach for gradient reconstruction provides higher accuracy than the Green-Gauss for most discretisation techniques [39]. However, if highly stretched meshes are used, this formulation fails to provide good estimates of gradients and also presents stability issues [39]. The Green-Gauss formulation presents an alternative solution to the unweighted/weighted Least-Square methods with similar accuracy, while maintaining robustness. Therefore, this technique is selected to reconstruct the gradient $\vec{\nabla}\mathbf{F}_j$ and the second derivatives $\vec{\nabla}(\vec{\nabla}\mathbf{F}_j)$ when high-order schemes are used.

The Green-Gauss formulation computes the gradient of any quantity $\mathbf{F}_j$ by integrating around the control-volume V_j with closed boundaries S. Figure 2 shows the stencil for Green-Gauss gradient

calculation for cell-centre discretisation in 2D. The components of the average gradients ($\vec{\nabla}\mathbf{F_1}$) over the control-volume V_j can be written as:

$$\begin{aligned}\frac{\partial \mathbf{F_1}}{\partial x} &= \frac{1}{V_j}\left(\mathbf{F_{12}}\mathbf{S_{12}}\overrightarrow{n}_{\mathbf{12}} + \mathbf{F_{13}}\mathbf{S_{13}}\overrightarrow{n}_{\mathbf{13}} + \mathbf{F_{14}}\mathbf{S_{14}}\overrightarrow{n}_{\mathbf{14}} + \mathbf{F_{15}}\mathbf{S_{15}}\overrightarrow{n}_{\mathbf{1}}\right)\overrightarrow{e}_{\mathbf{x}},\\ \frac{\partial \mathbf{F_1}}{\partial y} &= \frac{1}{V_j}\left(\mathbf{F_{12}}\mathbf{S_{12}}\overrightarrow{n}_{\mathbf{12}} + \mathbf{F_{13}}\mathbf{S_{13}}\overrightarrow{n}_{\mathbf{13}} + \mathbf{F_{14}}\mathbf{S_{14}}\overrightarrow{n}_{\mathbf{14}} + \mathbf{F_{15}}\mathbf{S_{15}}\overrightarrow{n}_{\mathbf{1}}\right)\overrightarrow{e}_{\mathbf{y}}.\end{aligned} \tag{7}$$

where $\mathbf{F_{12}}, \mathbf{F_{13}}, \mathbf{F_{14}}$, and $\mathbf{F_{15}}$ are the approximation of the variable $\mathbf{F}$ on the faces 12, 13, 14, and 15 with longitudes (2D) or surfaces (3D) $\mathbf{S_{12}}, \mathbf{S_{13}}, \mathbf{S_{14}}$ and $\mathbf{S_{15}}$ and unit normal vectors $\vec{n}_{12}, \vec{n}_{13}, \vec{n}_{14}$ and $\vec{n}_{15}$ and can be expressed as:

$$\begin{aligned}\mathbf{F_{12}} &= \frac{\mathbf{1}}{\mathbf{2}}(\mathbf{F_1} + \mathbf{F_2}), \quad & \mathbf{F_{13}} &= \frac{\mathbf{1}}{\mathbf{2}}(\mathbf{F_1} + \mathbf{F_3}),\\ \mathbf{F_{14}} &= \frac{\mathbf{1}}{\mathbf{2}}(\mathbf{F_1} + \mathbf{F_4}), \quad & \mathbf{F_{15}} &= \frac{\mathbf{1}}{\mathbf{2}}(\mathbf{F_1} + \mathbf{F_5}).\end{aligned} \tag{8}$$

Higher accuracy can be obtained using advance quadratures in space to evaluate $\mathbf{F}$ on the faces like the fourth-order introduced by McCorquodale *et al.* [15]. However, this formulation is more expensive and it requires adding a new layer of halo cells to the standard HMB. The components of the unit vectors $\vec{e}_x, \vec{e}_y$ are written in 2D as: $\vec{e}_x = [1\ 0]$ and $\vec{e}_y = [0\ 1]$, respectively.

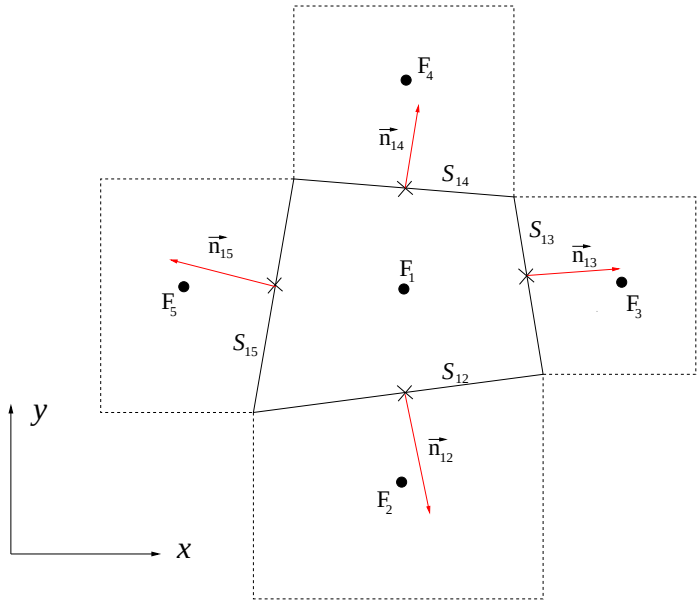

Fig. 2: Stencil for Green-Gauss gradient calculation for cell-centre discretisation in 2D.

B. Derivation of the high-order scheme

The high-order formulation requires optimal values of k_1 and k_2 to assure higher-order of accuracy. In this regard, we derive the order of accuracy of the scheme in 1D, considering the approxi-

mation of the derivates at the cell-centre as:

$$\int_{x-\frac{1}{2}}^{x+\frac{1}{2}} \frac{\partial \mathbf{F}}{\partial x} dx \approx \mathbf{F}^{\mathrm{L}}_{j+\frac{1}{2}} - \mathbf{F}^{\mathrm{L}}_{j-\frac{1}{2}} = \frac{1+k_2}{32}\mathbf{F}_{j+2} + \frac{7+8k_1-3k_2}{32}\mathbf{F}_{j+1} + \frac{11-12k_1+k_2}{16}\mathbf{F}_j + \frac{-19+12k_1+k_2}{16}\mathbf{F}_{j-1} + \frac{9-8k_1-3k_2}{32}\mathbf{F}_{j-2} + \frac{-1+k_2}{32}\mathbf{F}_{j-3} \quad (9)$$
$$= \mathbf{F}'_j \Delta x + \frac{1+6k_1}{24}\mathbf{F}'''_j \Delta x^3 + \frac{1-2k_1+k_2}{16}\mathbf{F}^{(4)}_j \Delta x^4 + O(\Delta x^5)$$

One can observe that this formula is at least 2nd-order accurate for all values of k_1 and k_2, while if $k_1 = -\frac{1}{6}$ and $k_2 = -\frac{4}{3}$, the approximation of the derivative at the cell-centre is 4th-order accurate, with no mechanism of dissipation. Moreover, a small amount of dissipation δ can be introduced to reduce spurious oscillation and at the same time maintain the high-order accuracy when k_2 is set to $-\frac{4}{3}+\delta$. A value of $\delta = 1 \times 10^{-4}$ is used throughout this work, which represents a compromise value between stability and level of accuracy obtained. The effect of δ on the solution is discussed later.

C. Fourier analysis

Fourier analysis is now used to assess the spectral properties of the proposed 4th-order scheme. If the flux is assumed to be a periodic sinusoidal function over a domain of unit length:

$$F(x) = e^{2\pi i \omega x} = e^{2\pi i \omega (j\Delta x)} \quad (10)$$

dissipation and dispersion errors can be quantified as functions of the grid wavenumber $\omega\Delta x$.

The phase error ($\overline{\omega}\Delta x$) of the Fourier transformation of (Eqn. 9) is given as:

$$\overline{\omega}\Delta x = \frac{45-16k_1-5k_2}{32}\sin(\omega\Delta x) + \frac{-8+8k_1+4k_2}{32}\sin(2\omega\Delta x) + \frac{1-k_2}{32}\sin(3\omega\Delta x) \quad (11)$$

Figure 3 shows the imaginary and real parts of the phase error or modified wavenumber of the derivative at the cell-centre, which are associated to dispersion and dissipation errors, respectively. The MUSCL-4 scheme (k_1=-1/6 and k_2=-4/3) is compared with the MUSCL-2 (2nd upwind scheme k_1=0), as well as the exact solution. It is observed that the proposed high-order scheme has a significantly higher spectral resolution than the standard MUSCL-2 schemes. Therefore, a wider range of wavenumbers can be accurately resolved for the MUSCL-4 schemes. Regarding the dissipation error, the MUSCL-4 scheme shows a considerable reduction compared to MUSCL-2. Moreover, at higher wavenumbers ($\omega\Delta x \geq 1.5$), the new scheme shows higher spectral resolution, which allows for capturing higher frequencies associated to the flow features (vortices, small length-scale waves).

D. Shock limiter

The HMB solver uses the alternative form of the Albada limiter [40] being activated in regions where a large gradients are encountered, mainly due to shock waves, avoiding the non-physical spurious oscillations. This limiter function is always differentiable.

Introducing the limiter function Φ, first-order and high-order schemes can be both combined. In fact, if $\Phi = 0$ the first-order is activated while if $\Phi = 1$ a higher-order scheme is activated, which is

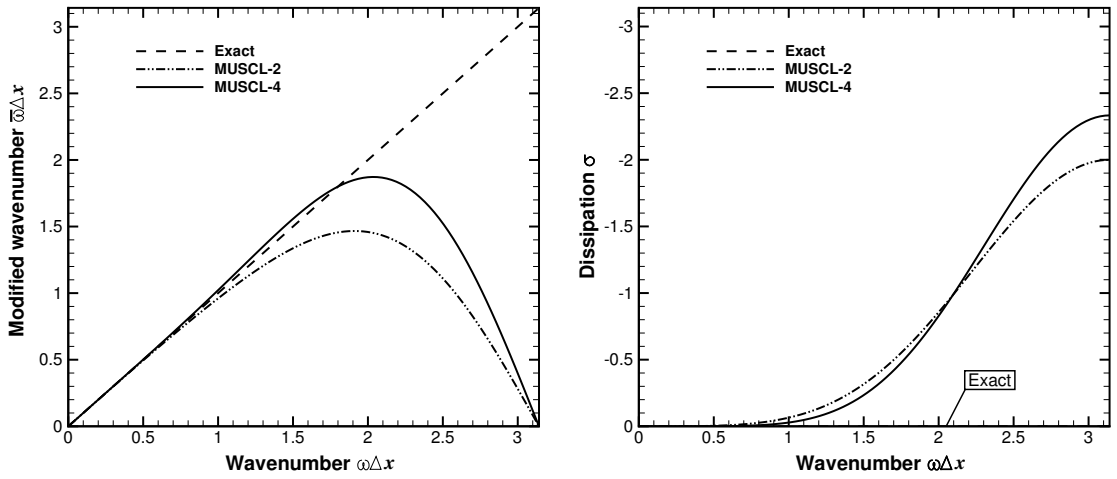

(a) Modified phase (imaginary part).

(b) Dissipation (real part).

Fig. 3: Fourier analysis for MUSCL-2 and MUSCL-4 schemes.

at least second-order of accuracy. When the fourth-order scheme is used, a limiter function should be applied to the high-order terms (see Michalak *et al.* [41]). However, the high CPU overhead added (30%-35%) in limiting high-order solutions, makes these limiters not yet suitable for high-order volume methods. Since no stability or convergence issues were observed for the variety of results presented here, the idea of not limiting the high-order term, but keeping the function Φ for the 2nd-order terms is put forward:

$$\begin{aligned}\mathbf{F}^{\mathrm{L}}_{j+1/2} &= \mathbf{F}_j + \Phi\left[\frac{k_1}{2}(\mathbf{F}_{j+1}-\mathbf{F}_j) + (1-k_1)\vec{\nabla}\mathbf{F}_j \bullet \vec{\mathbf{r}}_{f_j}\right] \\ &+\frac{1}{2}\left[\frac{k_2}{2}\left(\vec{\nabla}\mathbf{F}_{j+1}\bullet\vec{\mathbf{r}}_{f_j} - \vec{\nabla}\mathbf{F}_j\bullet\vec{\mathbf{r}}_{f_j}\right) + (1-k_2)\vec{\nabla}\left(\vec{\nabla}\mathbf{F}_j\bullet\vec{\mathbf{r}}_{f_j}\right)\bullet\vec{\mathbf{r}}_{f_j}\right].\end{aligned} \tag{12}$$

E. Memory Overhead

Eqns. 3 and 4 can be extended using Cartesian coordinates:

$$\begin{aligned}\mathbf{F}^{\mathrm{L}}_{j+1/2} &= \mathbf{F}_j + \frac{k_1}{2}(\mathbf{F}_{j+1}-\mathbf{F}_j) + (1-k_1)\vec{\nabla}\mathbf{F}_j\bullet\vec{\mathbf{r}}_{f_j} \\ &+\frac{1}{2}\left[\frac{k_2\Delta \mathrm{x}_{f_j}}{2}\left(\left(\frac{\partial \mathbf{F}}{\partial \mathrm{x}}\right)_{j+1} - \left(\frac{\partial \mathbf{F}}{\partial \mathrm{x}}\right)_j\right) + (1-k_2)\Delta \mathrm{x}_{f_j}\vec{\nabla}\left(\frac{\partial \mathbf{F}}{\partial \mathrm{x}}\right)_j\bullet\vec{\mathbf{r}}_{f_j}\right] \\ &+\frac{1}{2}\left[\frac{k_2\Delta \mathrm{y}_{f_j}}{2}\left(\left(\frac{\partial \mathbf{F}}{\partial \mathrm{y}}\right)_{j+1} - \left(\frac{\partial \mathbf{F}}{\partial \mathrm{y}}\right)_j\right) + (1-k_2)\Delta \mathrm{y}_{f_j}\vec{\nabla}\left(\frac{\partial \mathbf{F}}{\partial \mathrm{y}}\right)_j\bullet\vec{\mathbf{r}}_{f_j}\right] \\ &+\frac{1}{2}\left[\frac{k_2\Delta \mathrm{z}_{f_j}}{2}\left(\left(\frac{\partial \mathbf{F}}{\partial \mathrm{z}}\right)_{j+1} - \left(\frac{\partial \mathbf{F}}{\partial \mathrm{z}}\right)_j\right) + (1-k_2)\Delta \mathrm{z}_{f_j}\vec{\nabla}\left(\frac{\partial \mathbf{F}}{\partial \mathrm{z}}\right)_j\bullet\vec{\mathbf{r}}_{f_j}\right].\end{aligned} \tag{13}$$

$$
\begin{aligned}
\mathbf{F}^{\mathrm{R}}_{j+1/2} \;=\; & \mathbf{F}_{j+1} - \frac{k_1}{2}(\mathbf{F}_{j+1} - \mathbf{F}_j) - (1-k_1)\vec{\nabla}\mathbf{F}_{j+1} \bullet \vec{\mathbf{r}}_{f_{j+1}} \\
& + \frac{1}{2}\left[\frac{k_2 \Delta \mathrm{x}_{f_{j+1}}}{2}\left((\frac{\partial \mathbf{F}}{\partial \mathrm{x}})_{j+1} - (\frac{\partial \mathbf{F}}{\partial \mathrm{x}})_j\right) + (1-k_2)\Delta \mathrm{x}_{f_{j+1}}\vec{\nabla}\left(\frac{\partial \mathbf{F}}{\partial \mathrm{x}}\right)_{j+1} \bullet \vec{\mathbf{r}}_{f_{j+1}}\right] \\
& + \frac{1}{2}\left[\frac{k_2 \Delta \mathrm{y}_{f_{j+1}}}{2}\left((\frac{\partial \mathbf{F}}{\partial \mathrm{y}})_{j+1} - (\frac{\partial \mathbf{F}}{\partial \mathrm{y}})_j\right) + (1-k_2)\Delta \mathrm{y}_{f_{j+1}}\vec{\nabla}\left(\frac{\partial \mathbf{F}}{\partial \mathrm{y}}\right)_{j+1} \bullet \vec{\mathbf{r}}_{f_{j+1}}\right] \\
& + \frac{1}{2}\left[\frac{k_2 \Delta \mathrm{z}_{f_{j+1}}}{2}\left((\frac{\partial \mathbf{F}}{\partial \mathrm{z}})_{j+1} - (\frac{\partial \mathbf{F}}{\partial \mathrm{z}})_j\right) + (1-k_2)\Delta \mathrm{z}_{f_{j+1}}\vec{\nabla}\left(\frac{\partial \mathbf{F}}{\partial \mathrm{z}}\right)_{j+1} \bullet \vec{\mathbf{r}}_{f_{j+1}}\right].
\end{aligned}
\tag{14}
$$

These equations extrapolate the flow variables to both sides of the cell-face at $j+1/2$, so first and second derivatives and the vector distances $\vec{r}_{fj}$ and $\vec{r}_{fj+1}$ need to be computed (see Figure 4). For each direction and in 3D, 6 components of the vector distances are required ($\Delta \mathrm{x}_{f_j}, \Delta \mathrm{y}_{f_j}, \Delta \mathrm{z}_{f_j}$, $\Delta \mathrm{x}_{f_{j+1}}, \Delta \mathrm{y}_{f_{j+1}}\Delta, \mathrm{z}_{f_{j+1}}$), so 18 components are needed.

If two equation turbulence models are used, MUSCL-4 provides a memory overhead of 23%. Its breakdown is as follows: 3×7 and 6×7 doubles per cell for the first and second derivatives, respectively, and 18 extra doubles for the distance vectors in 81 doubles. This value needs to be added to the 350 doubles of the standard HMB [4, 42–44], resulting in the aforementioned 23% of memory overhead.

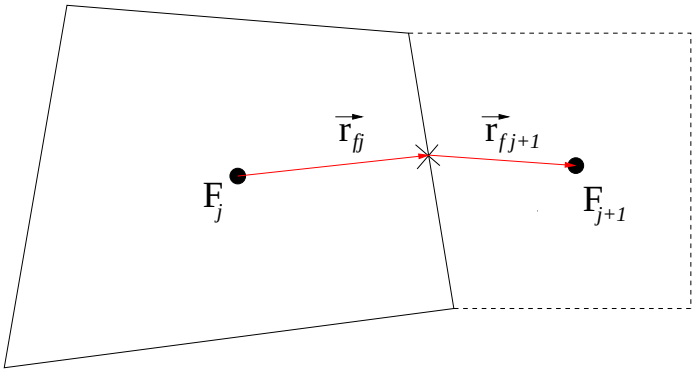

Fig. 4: Stencil for distance calculation for left and right states of j planes in 2D.

F. Implementation details

Some implementation details are listed here:

- Near solid bodies, the current implementation drops the order of the scheme to 2nd-order using 2 cells above the surfaces. Since the mesh is quite fine near solid bodies anyway, this is not a problem and allows for easy implementation of the scheme.
- At chimera boundaries, the current implementation drops the order of the scheme to 2nd-order. This was found to have a minimal overall effect.
- For parallel computations, the current implementation exchanges a halo of 2 cells for the first

and second derivatives. The standard HMB scheme only exchanges a halo of 2 cells for the solution.

- Most of the CPU penalties of the current implementation comes from additional data exchanged for parallel computations and extra effort is needed to calculate gradients with Green-Gauss's method.

- High-order derivatives are only applied to the inviscid flux, while the viscous flux remains second order.

- Due to the robustness of the scheme, there is not need to initialise the solution with a 2nd-order method solution.

III. Demonstration of the method and discussion of the results

In this section, numerical simulations with the high-order scheme are presented. The first part is devoted to the application of the scheme to Euler's equations. The convection of an isentropic vortex and the aerodynamic interaction between a vortex and a NACA-0012 aerofoil (blade-vortex interaction) are studied to verify the level of accuracy and resolution of flow features. Theoretical and numerical analyses of the truncation error are also included. The method is also applied to the steady, transonic, turbulent flow over the RAE2822 aerofoil, where the capability of the scheme in preserving accuracy for non-smooth solutions is investigated.

The second part concerns the application of the new scheme to three-dimensional turbulent steady and unsteady flows. Table 1 lists the test cases used in the validation of the present high-order scheme.

Table 1: List of test cases used in the validation of high-order methods.

Test Case	**Equations**	**Steady/Unsteady**
Isentropic vortex	Euler (2D)	Unsteady
BVI	Euler (2D)	Unsteady
RAE2822 aerofoil	Navier-Stokes (2D)	Steady
7AD rotor	Euler (3D)	Steady
S-76 rotor	Navier-Stokes (3D)	Steady
JORP propeller	Navier-Stokes (3D)	Steady
XV-15 tiltrotor	Navier-Stokes (3D)	Steady
UH-60A	Navier-Stokes (3D)	Unsteady
ERICA tiltrotor	Navier-Stokes (3D)	Unsteady

A. Vortex transported by uniform flow

The transport of a 2D isentropic vortex by a freestream flow is considered here. This problem has a well-known analytical solution [45], without numerical errors associated to dissipation and dispersion. Therefore, the capability of different numerical schemes in preserving the vortex shape and strength of the convected vortex can be evaluated. The computational domain is taken as $[0, 10] \times [0, 10]$ core-radii, where the initial flowfield is given as:

$$\begin{aligned} \rho =& \left[1 - \frac{(\gamma-1)b^2}{8\gamma\pi^2} e^{1-r^2}\right]^{\frac{1}{\gamma-1}}; \; p = \rho^\gamma \\ u =& u_\infty - \frac{b}{2\pi} e^{\frac{1-r^2}{2}} (y - y_c) \\ \mathrm{v} =& \mathrm{v}_\infty + \frac{b}{2\pi} e^{\frac{1-r^2}{2}} (x - x_c) \end{aligned} \tag{15}$$

with freestream velocity values set as $u_\infty = 0.2, v_\infty = 0$, respectively. The distance r from the vortex centre $(x_c, y_c) = (0, 0)$ to a point (x, y) is expressed as $r = \sqrt{(x - x_c)^2 + (y - y_c)^2}$ and $b = 5$ is the non-dimensionalised vortex strength. Periodic boundary conditions were applied in both directions. Here, ρ is fluid density, p static pressure, and u, v the two velocity components.

To evolve the solution in time, a fourth-order Runge-Kutta scheme (RK4) was employed, where the time-step selected was small enough to ensure conformity with the solution with the spatial resolution employed. Solutions were obtained on 32×32, 64×64, 128×128, and 256×256 equi-spaced Cartesian grids to study the spatial accuracy of different schemes, after the vortex travels a distance of two times the computational domain. Figure 5 shows the L_∞ error of the convergence rate for the MUSCL-2 (2nd-order upwind), MUSCL-3 (3rd-order upwind), and MUSCL-4 (4th-order upwind) schemes. The present 4th-order upwind scheme shows 4th-order error convergence, while the 3rd and 2nd-order upwind schemes give a 2nd-order error convergence. Similar convergence rates were also reported in the literature *et al.* [12].

Despite that the 2nd and 3rd-order upwind schemes present similar error convergence rates, the 3rd-order upwind scheme shows a faster convergence to the solution. It is interesting to note that the solutions obtained using the 4th order scheme have a significantly lower error than the 2nd and 3rd-order upwind schemes. This highlights the benefits of the higher-order method.

Figure 6 shows pressure contours of the isentropic vortex convection corresponding to the analytical and numerical solutions obtained by the MUSCL-2, MUSCL-3, and MUSCL-4 schemes on a 64×64 mesh. The solution obtained by the MUSCL-2 scheme shows significant dissipation of the vortex core and distortion of its shape. On the other hand, the MUSCL-4 scheme has the lowest dissipation error in comparison to all other schemes, which highlights the ability of this scheme in preserving the vortex shape and strength.

Comparisons of cross-sectional pressure contours computed by several schemes are given in Figure 7, using the 128×128 equi-spaced Cartesian grid. In addition to the numerical solutions obtained, the analytical solution is also included (represented by a solid line). It is seen that the MUSCL-2 scheme is not able to predict the peak of pressure mainly due to dissipation error (8.33%

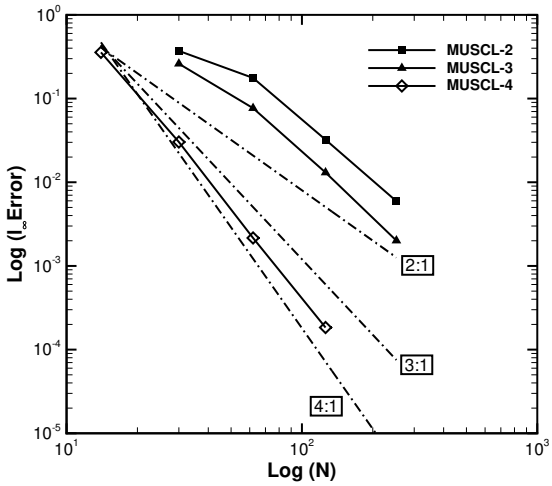

Fig. 5: Error convergences rate of MUSCL-2 (2nd-order upwind), MUSCL-3 (3rd-order upwind), and MUSCL-4 (4th-order upwind) schemes for vortex transport problem.

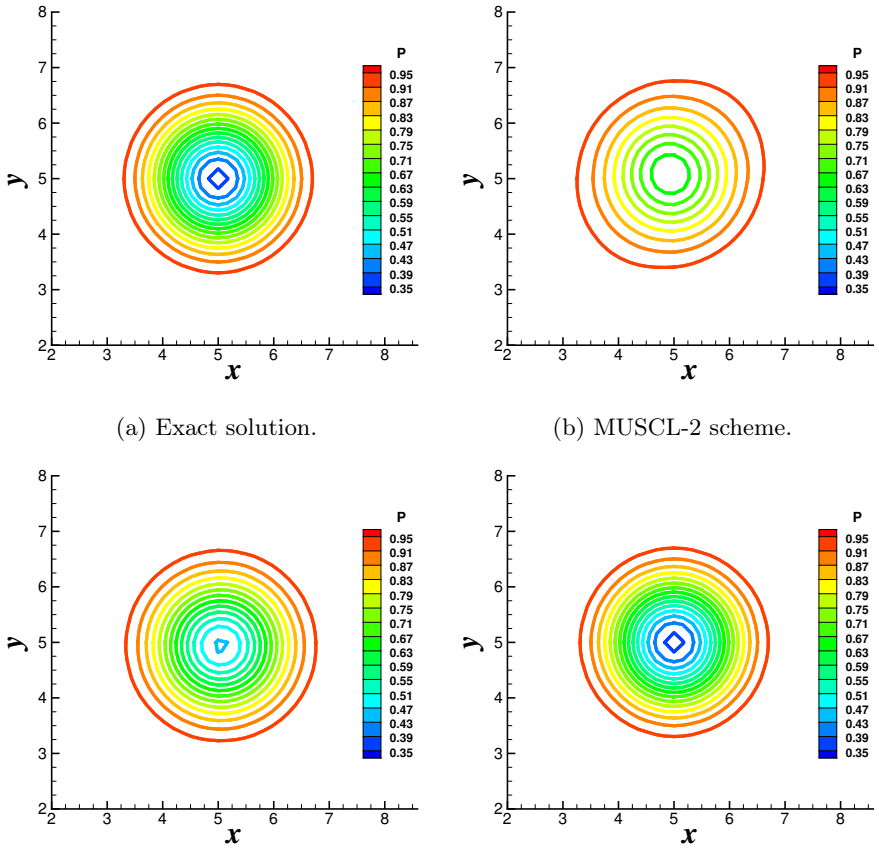

(a) Exact solution.

(b) MUSCL-2 scheme.

(c) MUSCL-3 scheme.

(d) MUSCL-4 scheme.

Fig. 6: Pressure contours for isentropic vortex convection after travelling two times the computational domain. Solutions were obtained on a 64×64 equi-spaced Cartesian grid.

discrepancy with the exact solution). By contrast, solutions using MUSCL-3 and MUSCL-4, show fair agreement with the exact solution with 2.95% and 0.26% discrepancies, respectively.

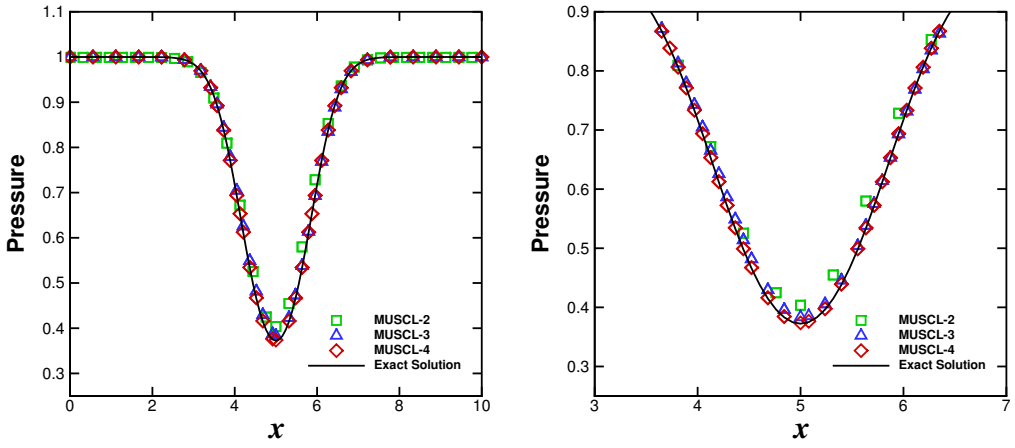

(a) Pressure distribution.

(b) Close view of the pressure distribution.

Fig. 7: Comparison of cross-sectional pressure contours computed by several schemes on a 128×128 equi-spaced Cartesian grid.

B. Blade-vortex interaction

The aerodynamic interaction between a vortex and a NACA-0012 blade, Blade-Vortex Interaction (BVI), is studied in this section. The BVI has been widely investigated in the past through theoretical research and experiments [46]. Numerical simulation of the BVI has been attempted using different methods, such as the indicial method [47], the cloud-in-cell method [48], or full potential methods [49]. Neither non-linearities of the flow associated to compressibility effects, nor rotational flow predictions are taken into account by these approaches, which may lead to errors in the flow predictions. By contrast, CFD methods allow a much better representation of the BVI mainly due to well-preserved vortices. Indeed, the vortex shape and strength are crucial for simulating BVI, and can be preserved using high-order schemes [50].

The test case presented here concerns the aerodynamic interaction between a vortex and a NACA-0012 aerofoil at freestream Mach number M_∞= 0.57, which refers to Case 1 in the experiments carried out by Lee and Bershader [51]. The surface pressure coefficients on the upper and lower sides of the blade were measured. Considering the set-up of the initial condition, a Scully-vortex with a non-dimensionalised vortex strength $\widehat{\Gamma} = -0.283$ and core radius $R_c = 0.018c$ was introduced in the flowfield, 1.5c ahead the aerofoil.

Two multi-block grids were built. The coarse mesh (G1) is composed by 42 blocks with a total size of 35,000 cells, while the medium mesh (G2) has a size of 70,000 cell. This mesh is refined close to the aerofoil surface and along the path travelled by the convected vortex. Views of the computational domain and the multi-block topology of the medium mesh are shown in Figures 8

(a) and (b), respectively.

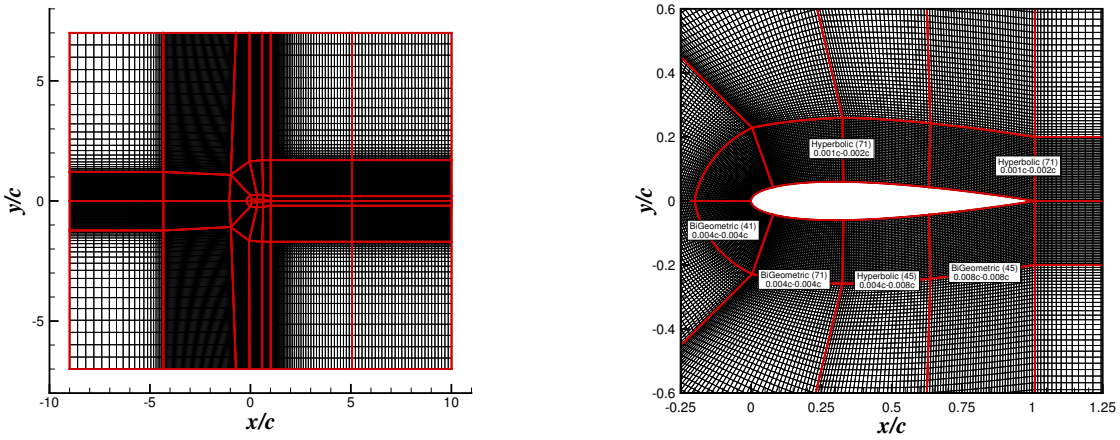

(a) Computational domain.

(b) Multi-block topology.

Fig. 8: Computational domain and multi-block topology of the medium grid (G2) used for the simulation of the head-on BVI, NACA-0012 aerofoil.

To march the unsteady solution in time, the RK4 scheme was used, and the effect of the spatial discretisation was evaluated through the use of the MUSCL-2 and MUSCL-4 schemes on the coarse and medium grids. No-slip wall and free-stream conditions were applied on the aerofoil surface and outer boundaries, respectively.

Comparisons of the time histories of the predicted and experimental surface pressure coefficients are given in Figure 9. Probes on the upper and lower sides of the aerofoil surface were considered, corresponding to $x/c = 0.02$, 0.05, and 0.10. Regarding the probes located on the upper surface (see Figures 9 (a),(c), and (e)), results obtained with the MUSCL-4 on the coarse grid (G1) show a higher resolution of the suction peak C_P compared with standard MUSCL solutions using the medium grid (G2). The low dissipation of the present high-order schemes gives a much better representation of the blade-vortex interaction. Comparisons of the C_P on the lower side (see Figures 9 (b),(d), and (f)) also support this idea, where the small features of the flowfield were only captured by the MUSCL-4 scheme.

The overall agreement between CFD and test data is as reported by other authors in the literature using different schemes including the Compressible Vorticity Confinement Method (CVCM) [52].

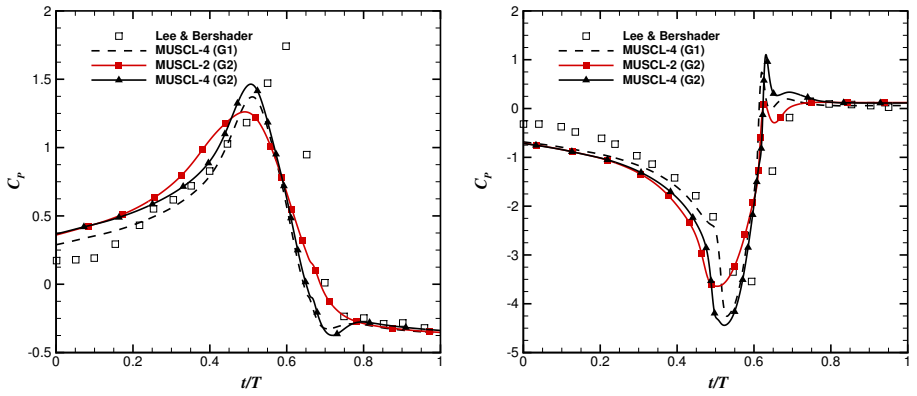

(a) Upper surface, $x/c = 0.02$.

(b) Lower surface, $x/c = 0.02$.

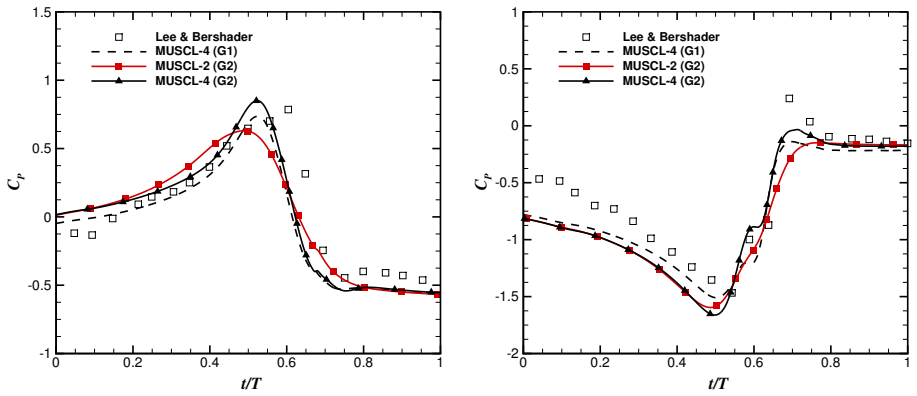

(c) Upper surface, $x/c = 0.05$.

(d) Lower surface, $x/c = 0.05$.

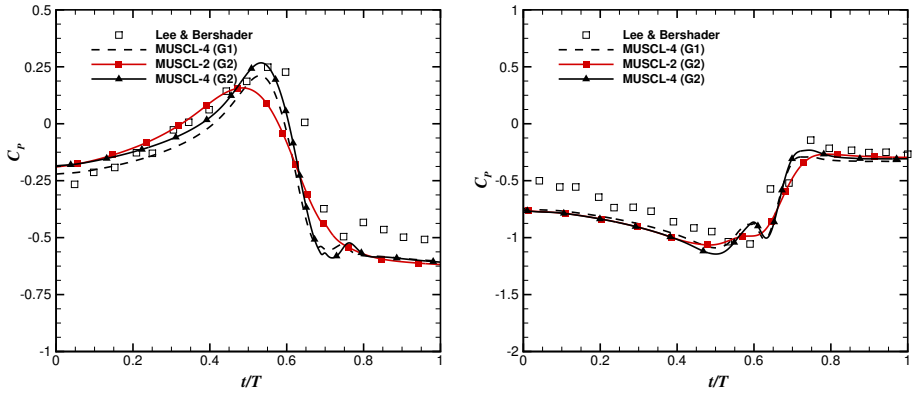

(e) Upper surface, $x/c = 0.10$.

(f) Lower surface, $x/c = 0.10$.

Fig. 9: Influence of the high spatial accurately numerical schemes on the time history of the surface pressure coefficient. Head-on BVI problem, NACA-0012 aerofoil, inviscid calculations, M_∞=0.5, Scully-model with $\widehat{\Gamma}$=-0.283 and R_c=0.018.

C. Turbulent flow over the RAE2822 aerofoil

The application of the MUSCL-4 scheme to the steady, transonic, turbulent flow over the RAE2822 aerofoil is presented here. This test case is designed to gain information on how the shock limiter works with the new high-order scheme. In this regard, results are compared with available experimental data in terms of the surface pressure coefficient. The case considered here corresponds to Case 6 in Cook *et al.* [53], where the freestream Mach and Reynolds numbers were set to 0.731 and 6.5 million (based on the mean aerodynamic chord) with an angle of attack of 2.51°. For this particular case, the Mach number and angle of attack were corrected by Tatsumi *et al.* [54] to account wind tunnel effects. The flow solutions were computed solving the RANS equations, coupled with Menter's k-ω SST turbulence model [55].

A C-H mesh topology was employed with the outer boundaries located 50 chord lengths away. The mesh had 371 nodes on the aerofoil surface along with 91 points in the normal direction following an exponential distribution (the mesh wall distance was $4 \times 10^{-6} c_{\text{ref}}$), which resulted in a grid size of 93,000 cells.

The numerical solutions were obtained using the MUSCL-2 and MUSCL-4 schemes, and the RK4 scheme to march the solution in time to steady state. Figure 10 (a) shows contours of pressure around the transonic RAE2822 aerofoil. The shock on the upper surface of the aerofoil is visible. Figure 10 (b) shows a comparison of C_P between the MUSCL-4 scheme and experiments [53] on the aerofoil surface. Despite small discrepancies found in the predicted suction peak, an excellent agreement is observed between the numerical simulation and the experimental data, where the position of the shock is well captured. Figure 11 shows a comparison of skin friction coefficient between both schemes and experiments [53]. Both schemes predict similar trends on the upper and lower surface of the aerofoil, and good agreement is observed.

D. 7AD helicopter blade

The flow around the 7AD four-bladed main rotor is now used to demonstrate the performance of the MUSCL-4 scheme on a three-dimensional flow and on a coarse mesh with the Euler equations. In fact, the lack of natural dissipation mechanism of Euler equations (such as viscosity in the Navier-Stokes equations) makes it easier to analyse the impact of the numerical dissipation associated to spatial discretisation in preserving the vortex core. Numerical simulations using the MUSCL-2 are also undertaken for comparison.

The 7AD main rotor consists of four blades of aspect ratio (R/c) of 15. The blades are comprised of aerofoils of the OA2XX series of 9% thickness. The 7AD rotor blade had 2.1 m radius, 0.14 m chord, linear twist distribution, and was equipped with anhedral tips with parabolic taper [56].

Experiments were conducted at the DNW wind tunnel within the European project HELISHAPE [57]. The hover conditions considered here employ a blade-tip Mach number $M_{\text{tip}} = 0.66$, blade pitch angle of 7.5 degrees and blade loading coefficient C_T/σ=0.076, where σ represents the rotor solidity.

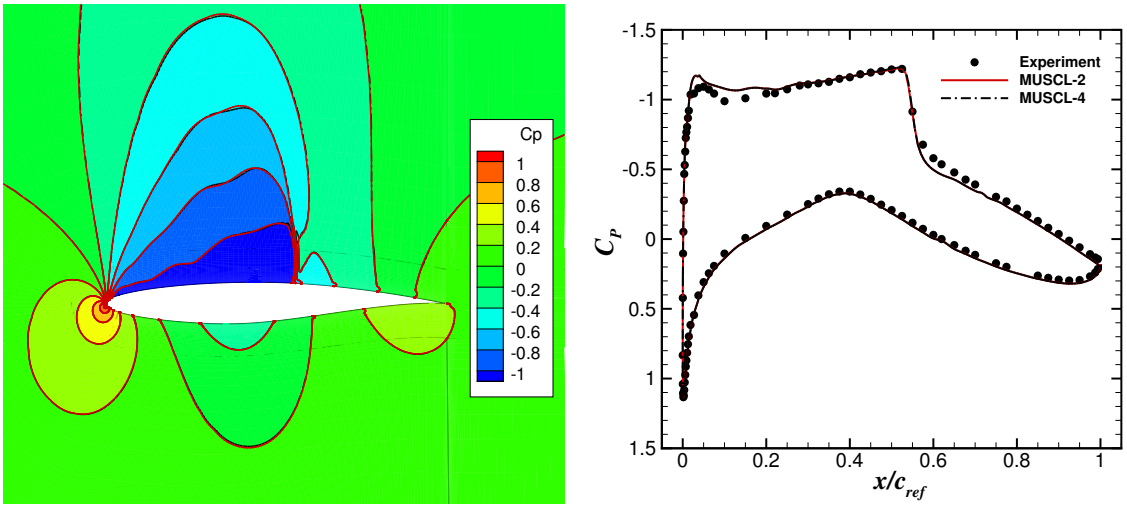

(a) Pressure contours.

(b) C_P profile.

Fig. 10: (a) Contours of pressure and (b) C_P profile comparison between CFD and experiments [53] around the RAE2822 aerofoil. Red and black lines correspond to MUSCL-2 and MUSCL-4 solutions, respectively.

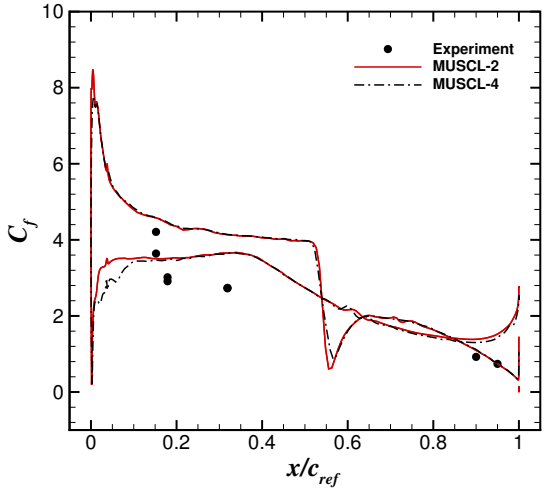

Fig. 11: Skin friction coefficient comparison between CFD and experiments [53] around the RAE2822 aerofoil. Red and black lines correspond to MUSCL-2 and MUSCL-4 solutions, respectively.

As the 7AD is a four-bladed rotor, only a quarter of the domain was meshed, assuming periodic conditions for the flow in the azimuthal direction. Outer boundaries were located $2R$ (above) and $4R$ (below) away of the blade tip, while the mesh extended by 3 rotor radii ($3R$) in the radial direction. A C-topology around the leading edge of the blade was selected, whereas an H-topology was employed at the trailing edge of the blade, resulting in a coarse mesh with dimensions of 1 million nodes per blade. The domain was decided based on previous experience [34], and the mesh

density is coarse.

Figure 12 shows comparisons of C_P profiles between CFD and experiment [57] at radial stations $r/R = 0.5$, 0.7, and 0.915 for MUSCL-2 and MUSCL-4 schemes. At inboard stations ($r/R = 0.5$ and 0.7) both schemes are in close agreement with the experiments with negligible differences between them. At the most outboard station ($r/R = 0.915$), however, the effect of the scheme becomes more noticeable on the prediction of the suction peak. Table 2 reports the predicted suction peak C_P for both schemes as well as the experimental one for the most outboard stations. Especially, for $r/R = 0.915$, MUSCL-4 appears to agree better with test data even if there is scatter between measurements obtained on each of the four blades as can be seen by the test data where four symbols are present at each x/c_{ref} station.

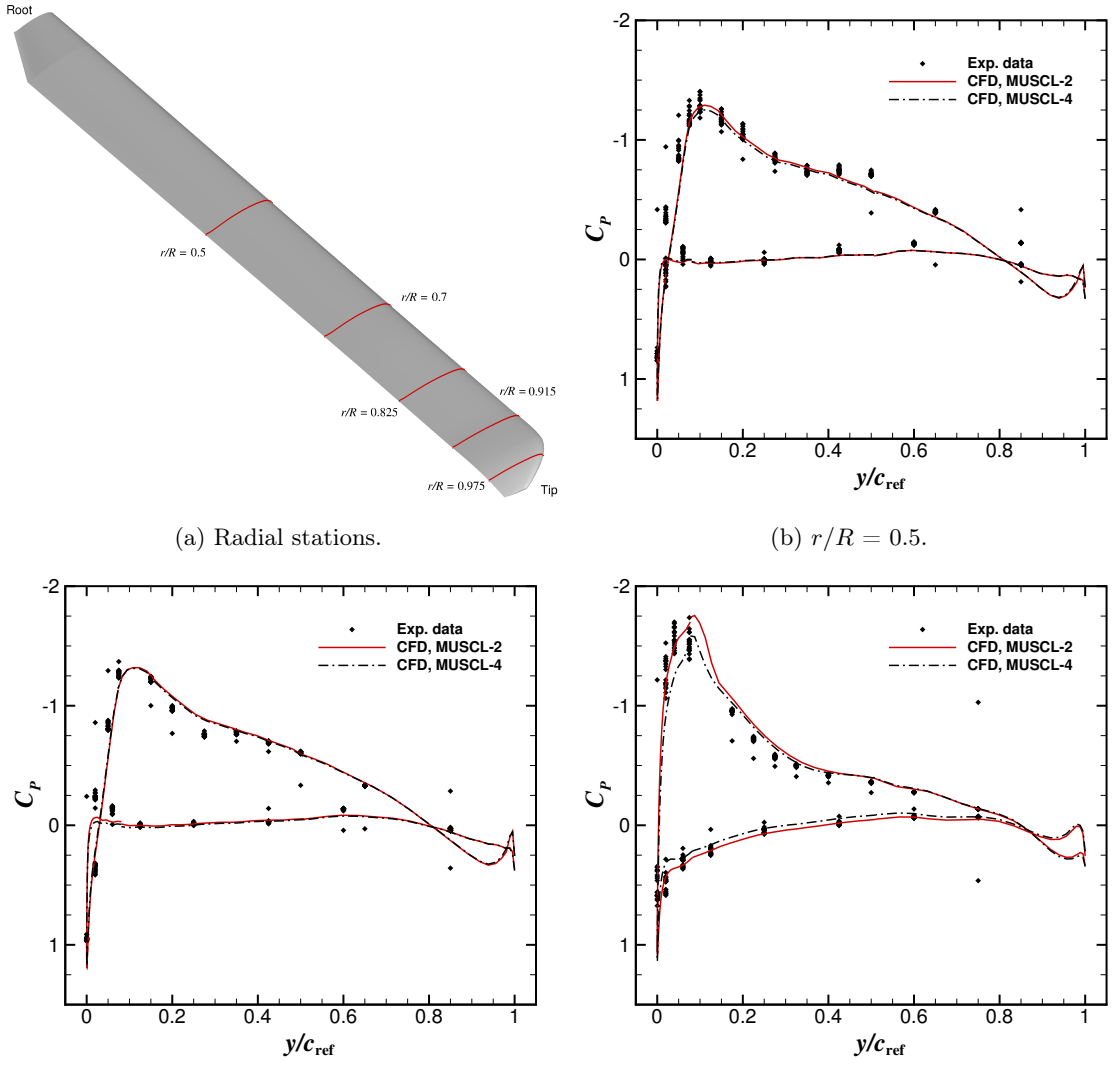

(a) Radial stations.

(b) $r/R = 0.5$.

(c) $r/R = 0.7$.

(d) $r/R = 0.915$.

Fig. 12: C_P profile comparisons between experiment [57] and MUSCL-2 and MUSCL-4 schemes.

Table 2: Predictions and experimental suction peak C_P for the full-scale 7AD rotor.

	Experiment	**CFD**	
r/R		**MUSCL-2**	**MUSCL-4**
		(% change)	(% change)
0.915	-1.47	-1.75 (19.04)	-1.58 (7.48)
0.975	-1.20	-1.82 (51.66)	-1.70 (41.66)

Figure 13 shows the wake visualisation of the 7AD rotor using iso-surfaces of $\bar{Q}$-criterion. The quantity Q is defined as follows:

$$Q = \frac{1}{2}(\Omega_{ij}\Omega_{ij} - S_{ij}S_{ij}), \tag{16}$$

where Ω_{ij} and S_{ij} are the antisymmetric and symmetric part of the velocity gradient, respectively:

$$\Omega_{ij} = \frac{1}{2}\left(\frac{\partial u_i}{\partial x_j} - \frac{\partial u_j}{\partial x_i}\right), \quad S_{ij} = \frac{1}{2}\left(\frac{\partial u_i}{\partial x_j} + \frac{\partial u_j}{\partial x_i}\right). \tag{17}$$

The quantity Q has the dimensions of a velocity squared divided by a length squared, and it is therefore nondimensionalised in HMB as follows:

$$\bar{Q} = Q\left(\frac{L_{\text{ref}}}{V_{\text{ref}}}\right)^2 = Q\left(\frac{c_{\text{ref}}}{V_{\text{tip}}}\right)^2. \tag{18}$$

The capability of both schemes in preserving the helical tip vortex in the wake can thus be assessed. It is observed that the MUSCL-2 scheme can only resolve the first vortex passage (wake age of 90π radians). The MUSCL-4 scheme shows a completely preservation of the first and second vortex passage (wake age of 180π radians).

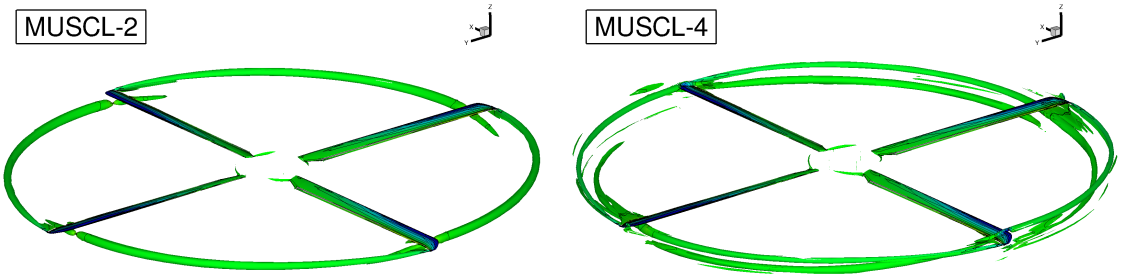

(a) Wake flow using MUSCL-2 scheme.

(b) Wake flow using MUSCL-4 scheme.

Fig. 13: Wake flowfield for the 7AD rotor using $\bar{Q}$-criterion ($\bar{Q} = 0.05$) obtained with MUSCL-2 (left) and MUSCL-4 (right) schemes.

Figure 14 shows the vorticity field near the tip vortex and the vortex of the preceding blade generated by the hovering 7AD rotor in azimuthal planes located behind the blade. The visualisations highlight the ability of the present high-order scheme to capture and preserve the wake vortices. For instance, vorticity values of the tip vortex core computed with MUSCL-2 presents a reduction of the core vorticity by almost 20% with respect to the MUSCL-4 results.

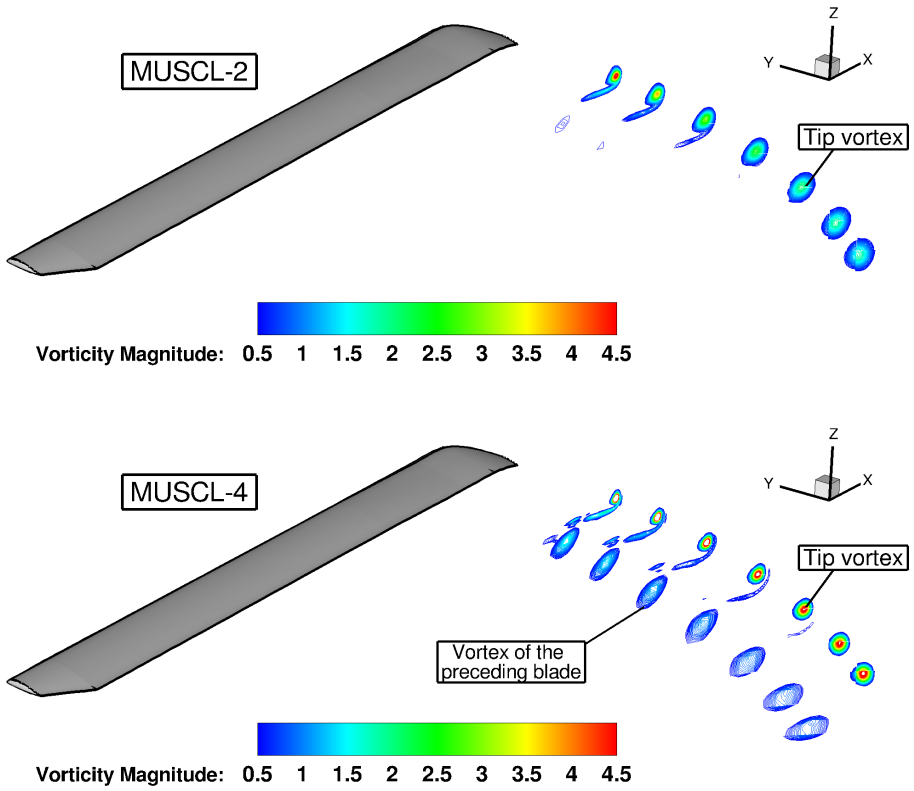

Fig. 14: Vorticity field of the 7AD hovering rotor using MUSCL-2 (top) and MUSCL-4 (bottom) schemes.

E. S-76 helicopter blade in hover

In this section, the flow around the 1/4.71 scale S-76 rotor blade, in hover, is computed using the MUSCL-2 and MUSCL-4 schemes. Due to the public availability of the case, and data sets with various tip shapes, the AIAA Applied Aerodynamics Rotor Simulations Working Group [58–61] was established in 2014 to evaluate the current state-of-the-art performance prediction using different CFD solvers and methods for the same blade geometry. Therefore, this blade has been extensively studied [62–66] and represent a unique benchmark for the validation of MUSCL-4 scheme on hovering helicopter rotors.

The four-bladed S-76 model rotor, of 1/4.71 scale, has -10° of non-linear twist, and three aerofoil sections comprise its planform: the SC-1013-R8 is used from the root of the blade up to 18.9% R, the SC-1095-R8 aerofoil is used from 40% R to 80% R, and the SC-1095 aerofoil is used from 84% R to the tip. For this study, the planform of the S-76 model rotor with 60% taper and 35° swept tip is selected at a scale of 1/4.71. The main characteristics of the model rotor blades are summarised in Table 3.

The blade-tip Mach number was set to 0.65 and three blade collective angles were considered,

Table 3: Geometric properties of the 1/4.71 scale S-76 rotor [67].

Parameter	Value
Number of blades, N_b	4
Rotor radius, R	56.04 inches
Reference blade chord, c_{ref}	3.1 inches
Aspect ratio, R/c_{ref}	18.07
Rotor solidity, σ	0.0704
Non-linear twist, Θ	-10°

corresponding to low, medium, and high thrust. The Reynolds number, based on the reference blade chord of 3.1 inches and on the tip speed, was 1.18×10^6. All flow solutions were computed by solving the RANS equations, coupled with Menter's k-ω SST turbulence model [55]. The flow equations were integrated with the implicit dual-time stepping method of HMB.

A mesh generated using the chimera technique was used for the design study of the S-76 rotor, composed of a periodic background mesh and a component mesh for the blade (see Figure 15 (a)). As the S-76 is a four-bladed rotor, only a quarter of the domain was meshed. A C-topology around the leading edge of the blade was selected, whereas an H-topology was employed at the trailing edge of the blade (see Figure 15 (b)). Coarse and medium grids were built. Table 4 shows the breakdown in terms of number of cells (per blade) used for the background, and for the body-fitted meshes around the S-76 rotor blade. Because the number of cells of the foreground mesh is sufficient to accurately capture the loads on the blade, the second-order scheme is used in this level, while MUSCL-4 scheme is activated at the background level.

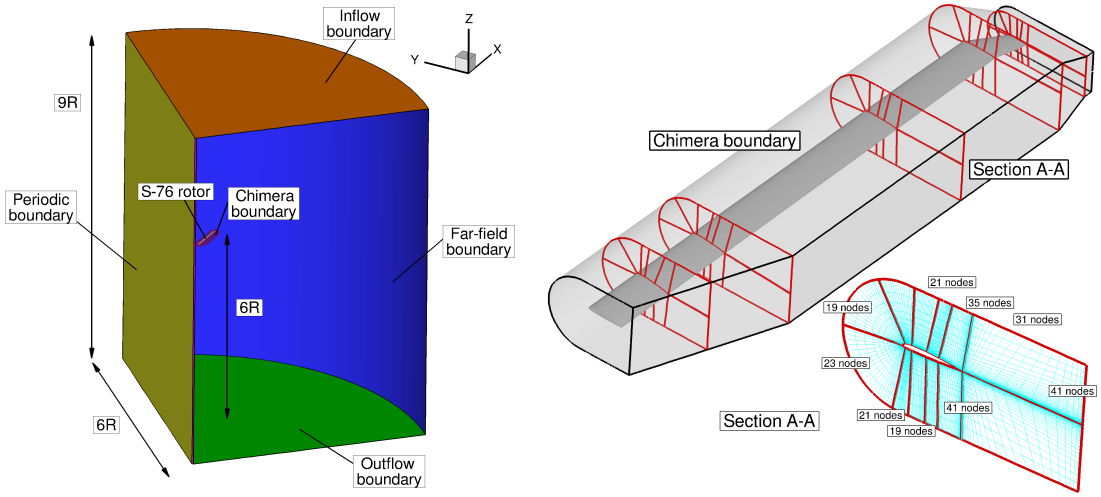

(a) Computational domain.

(b) S-76 rotor mesh.

Fig. 15: Computational domain and boundary conditions employed (left) and detailed view of the body-fitted S-76 rotor mesh (right).

Table 4: Mesh size in million cells for the S-76 rotor mesh.

	Coarse Mesh	**Mesh**
Background mesh size	2 million	3.5 million
Blade mesh size	3 million	4 million
Overall mesh size	5 million	7.5 million
Wall distance	$1.0 \times 10^{-5} c_{\text{ref}}$	$1.0 \times 10^{-5} c_{\text{ref}}$

The effect of the spatial discretisation on the figure of merit and torque coefficient as a function of the blade loading coefficient C_T/σ is shown in Figures 16 (a) and (b), respectively. Vertical lines are labelled as empty (3,177 kg, C_T/σ= 0.06) and maximum gross (5,307 kg, C_T/σ= 0.1) weight, define the hovering range of the S-76 helicopter rotor. CFD solutions were obtained with the MUSCL-2 and MUSCL-4 schemes using a coarse (red and black lines, respectively) and medium grids (green solid lines and pink deltas, respectively). The test data of Balch and Lombardi [67] are represented by opened squares. The ability to resolve the vortex structure at the background level is key for accurate predictions of the loading on the blade. Hence, half million cells were added to the new background mesh (see Table 4). Consequently, the medium mesh shows a better agreement at low, medium, and high thrust coefficients with the test data of Balch and Lombardi [67]. Results obtained with the MUSCL-4 scheme and the coarse mesh show a very good agreement with the experimental data and with the MUSCL-2 scheme results on the medium grid.

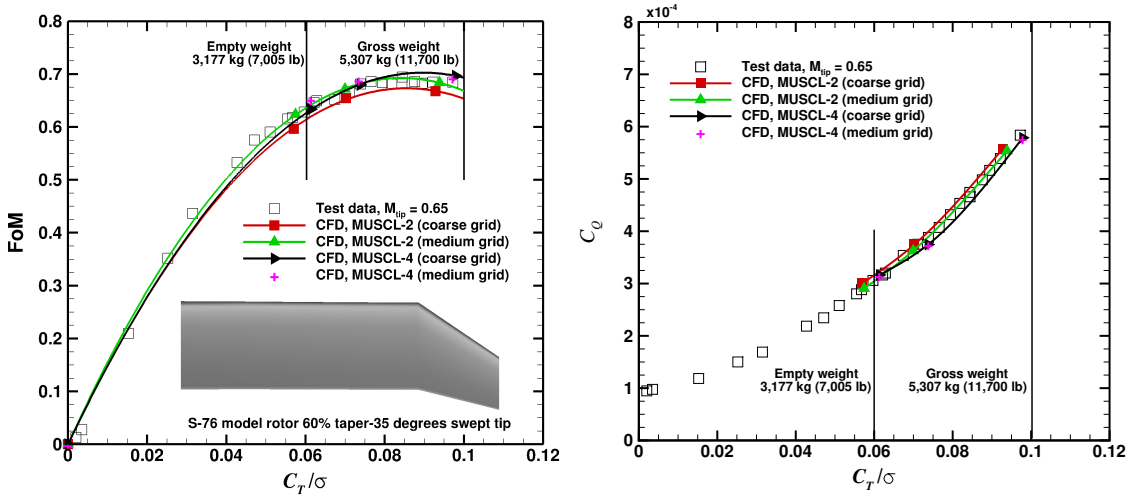

(a) FoM - C_T/σ.

(b) C_Q - C_T/σ.

Fig. 16: Effect of the MUSCL-2 and MUSCL-4 schemes on the figure of merit (left) and torque coefficient (right) for the 1/4.71 scale S-76 rotor blade.

F. CPU and memory overheads

Table 5 reports the computational run-time in work units (non-dimensional time requires to compute 1 implicit iteration of MUSCL-2) per implicit iteration for the S-76 rotor blade when MUSCL-2 and MUSCL-4 schemes are used on the coarse and medium grids, respectively (see Table 4). Solutions were computed on 8 cores of the high performance cluster of Glasgow University, Jupiter, comprised of Intel Xeon E5620 3.2 GHz processors. For both meshes, a CPU overhead of about 22% is found. Implicit iterations were used, so the time required to compute the pre-conditioner matrix and resolve the linear system (when using the same number of Conjugate Gradient steps) should be similar for both schemes. So, the extra CPU time required by the MUSCL-4 scheme is shared across five main jobs: computing the cell-centre values for the first and second derivatives using Green-Gauss's method, exchanging data between processors for the first and second derivatives, and computing the new left and right states (high-order correction terms). Regarding the coarse mesh, CPU overheads of 0.5% and 0.95% were found for computing first and second derivatives, showing a small penalty. Halo data exchanges, however require: 1.5% and 4.2% for the first and second derivatives, respectively. For this case, penalties of 8.25% and 5.6% need to be paid when computing the new residual Jacobian matrix with the high-order correction terms, and resolve the linear systems, respectively. CPU overheads of 0.6% (first derivative calculation), 1.16% (second derivative calculation), 1.66% (data exchange for the first derivative), and 5.23% (data exchange for the second derivative) were reported for the medium mesh. Run-times associated to the computation of the first and second derivatives do not show a strong dependency on either the mesh size nor the parallel process, while the halo data exchange for the first and second derivatives seems to be more affected. This is due to the fact that the parallelisation technique used for the halo data exchange of both derivatives follows the same logic that the standard HMB with the solution vector. Instead of sharing between processors a single vector of 9 variables $\left(\frac{\partial F}{\partial x}, \frac{\partial F}{\partial y}, \frac{\partial F}{\partial z}, \frac{\partial^2 F}{\partial x^2}, \frac{\partial^2 F}{\partial y^2}, \frac{\partial^2 F}{\partial z^2}, \frac{\partial^2 F}{\partial xy}, \frac{\partial^2 F}{\partial xz}, \frac{\partial^2 F}{\partial yz}\right)$, each variable is exchanged individually.

Table 5: Computational run-time for the S-76 rotor blade with MUSCL-2 and MUSCL-4 schemes on the coarse and medium meshes.

Mesh	**Scheme**	**CPU**	**CPU [%]**
		work units/iteration	
Coarse Mesh (5 million cells)	MUSCL-2	1	1
	MUSCL-4	1.21 (21%)	1.21 (21%)
Medium Mesh (7.5 million cells)	MUSCL-2	1	1.38 (38%)
	MUSCL-4	1.22 (22%)	1.68 (68%)

The computational efficiency of the MUSCL-4 schemes can be now demonstrated. For this case, the MUSCL-4 scheme is more expensive than the MUSCL-2 scheme on the same grid ($\sim$ 22%). When comparing solutions, however, with the similar errors, the MUSCL-4 scheme is less

expensive. As discussed before, MUSCL-2 on the medium mesh provides similar blade loads than MUSCL-4 on the coarse mesh (see Figure 16). However, the MUSCL-4 on the coarse mesh is 14.7% less expensive that the MUSCL-2 on the medium mesh.

G. JORP propeller blade

As a means of evaluating the high-order method in accurately predicting airloads for modern propeller blades at high cruise speed, the Joint Open Rotor Propeller (JORP) propeller blade is considered [68]. A single row of six blades were built with an unswept planform in conjunction with a minimum interference spinner.

Like for the S-76, a mesh using the chimera technique is used here, composed of a periodic background mesh, where MUSCL-4 was activated, and a component mesh for the blade (MUSCL-2 scheme was activated). Table 6 shows the number of cells (per blade) used for the background mesh (6.3 million cells), and for the foreground (3.1 million cells).

Table 7 shows the condition employed for the axial flight. The cruise condition was modelled at 0 ft (ISA+0°), with a blade-tip Mach number of 0.529 and advance ratio 1.309. The Reynolds number for this case was 1.163×10^6, based on the reference blade chord and rotor tip speed (with no account for the advance velocity). The blade pitch angle θ_{70} was set to 60° degrees.

Table 6: Mesh size in million cells for the JORP rotor mesh.

	Mesh
Background mesh size	6.3 million
Blade mesh size	3.1 million
Overall mesh size	9.4 million
Wall distance	$1.0 \times 10^{-5} c_{\text{ref}}$

Table 7: Flow conditions for the propeller blade.

Parameter	**Value**
Blade-tip Mach number, M_{tip}	0.54
Freestream Mach number, M_∞	0.69
Advance ratio, μ	1.309
Reynolds number, Re	1.163×10^6
Blade pitch angle, θ_{70}	60°
Turbulence model	k-ω SST

All flow solutions were computed by solving the RANS equations, coupled with Menter's k-ω SST turbulence model [55]. The flow equations were integrated with the implicit dual-time stepping method of HMB, using a pseudo-time Courant–Friedrichs–Lewy CFL equal to 3. Typically, 40,000 iterations were necessary to drop the residual by almost 6 orders of magnitude for the flow solutions.

As discussed earlier, in 1D the approximation of the derivative at the cell-centre is 4th-order accurate, with no mechanism of dissipation. Moreover, a low dissipation δ can be introduced to reduce spurious oscillation and at the same time maintain the high-order accuracy. This allows us to use MUSCL-4 without a lower-order solution to initiate the flow, keeping the robustness of the standard HMB solver as shown in Figure 17.

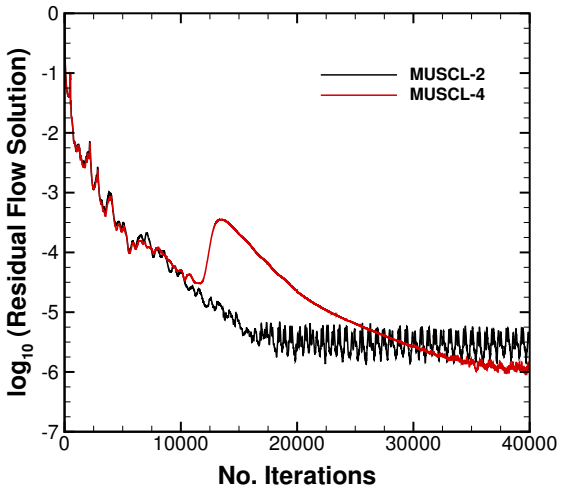

Fig. 17: Residual of the flow solution of the JORP propeller blade as function of the number of iterations for the MUSCL-2 and MUSCL-4 schemes.

Figure 18 shows C_P profile comparisons between experimental data [68] and HMB at the radial stations $r/R = 0.6$ and 0.9. The CFD results obtained with both schemes provide good resolution of the airloads of the propeller blade for this demanding flight condition, and are almost identical between the two methods. The use of a thin aerofoil in conjunction with a moderate taper tip shape tends to limit the compressibility effects at the tip region encountered in this flight condition at high advance ratio.

Figure 19 shows iso-surfaces of $\bar{Q}$-criteria obtained with the MUSCL-2 (left) and MUSCL-4 (right) solutions. It is clear that the helical vortex filaments trailing from the tip-blade are preserved much better by the MUSCL-4 scheme. The same is seen for the blade root vortices.

H. CPU and memory overheads

Table 8 reports the computational run-time in work units per implicit iteration for the JORP propeller blade when MUSCL-2 and MUSCL-4 schemes are used on the same grid. Solutions were computed on 8 cores of the high performance cluster of Glasgow University Jupiter, comprised of Intel Xeon E5620 3.2 GHz processors. This case has a lower penalty compared to the S-76, with a CPU overhead of about 13%. CPU overheads of 0.7% and 1.3% are reported for the computation of the first and second derivatives. Halo data exchanges have penalties of 1.6% and 4.17% for the first and second derivatives, respectively. Computing the new residual Jacobian matrix with the high-

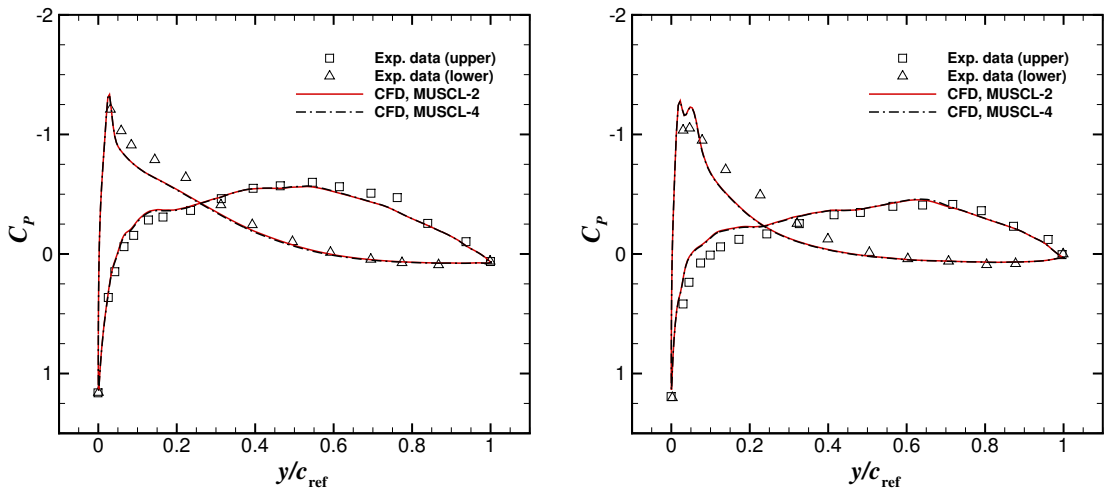

(a) $r/R = 0.6$ (b) $r/R = 0.9$.

Fig. 18: C_P profile comparisons between experimental data [68] and HMB at radial stations r/R = 0.6 (left) and 0.9 (right).

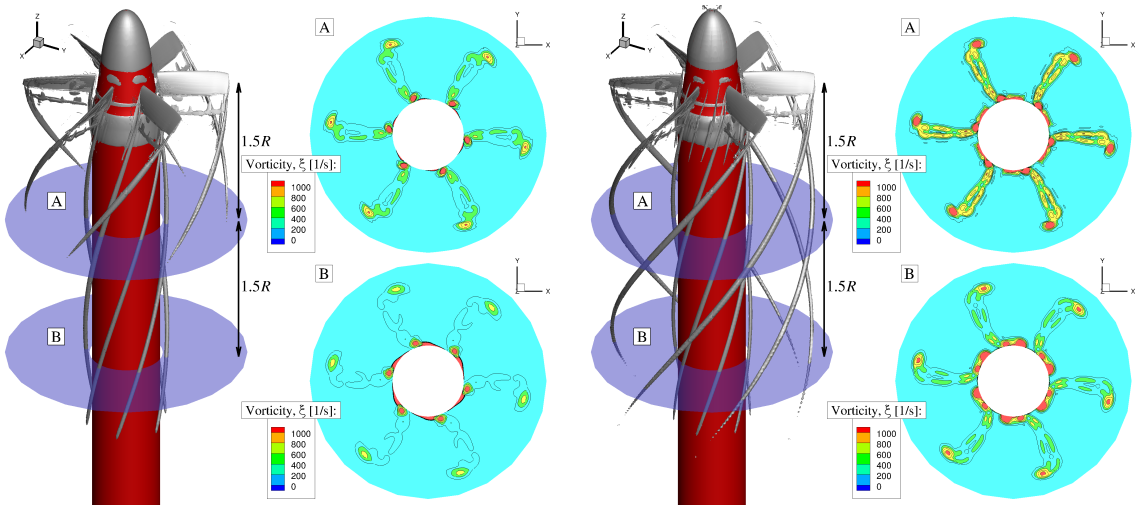

(a) Wake flow using MUSCL-2 scheme. (b) Wake flow using MUSCL-4 scheme.

Fig. 19: Wake flowfield for the JORP propeller blade using $\bar{Q}$-criterion ($\bar{Q} = 0.1$) obtained with MUSCL-2 (left) and MUSCL-4 (right) schemes.

order correction terms and resolving the linear systems add 4.1% and 1.3% in CPU, respectively. Like for the S-76, a memory overhead of 23% is added when the MUSCL-4 scheme is used. Nevertheless, solutions obtained with MUSCL-4 provide better wake resolution with only a small penalty in CPU and memory for this medium mesh of 9 million cells.

Table 8: Computational run-time for the JORP propeller blade with MUSCL-2 and MUSCL-4 schemes.

Mesh	**Scheme**	**CPU work units/iteration**
9.4 million cells mesh	MUSCL-2	1
	MUSCL-4	1.13 (13%)

I. XV-15 tiltrotor blade

This section demonstrates the performance of the MUSCL-4 scheme when used with chimera grids for a three-dimensional tiltrotor flow. This highly loaded rotor produces strong wakes, thus the resolution of which may benefit from a higher-order scheme.

The flow around the three-bladed XV-15 rotor [69] is solved in hover by casting the equations as a steady-state problem in a noninertial reference frame. The MUSCL-4 scheme is compared with MUSCL-2 in terms of integrated airloads (FoM, C_T, and C_Q), visualisation of the wake flow features, and wake structure. All flow solutions were computed using the RANS equations and Menter's k-ω SST turbulence model [55]. The flow equations were integrated with the implicit dual-time stepping method of HMB.

The three-bladed XV-15 rotor comprises NACA 6-series, five-digit aerofoil sections, and its main characteristics [69] are summarised in Table 9. Regarding test conditions, the blade-tip Mach number was set to 0.69, and five blade collective angles were considered ($\theta_{75} = 3°, 5°, 7°, 10°$, and $13°$), corresponding to low, medium, and high disc loadings. The Reynolds number, based on the reference blade chord of 14 inches and on the tip speed, was 4.95×10^6.

Table 9: Geometric properties of the full-scale XV-15 rotor [69].

Parameter	**Value**
Number of blades, N_b	3
Rotor radius, R	150 inches
Reference blade chord, c_{ref}	14 inches
Aspect ratio, R/c_{ref}	10.71
Rotor solidity, σ	0.089
Non-linear twist, Θ	-40.25°

The computational domain includes a cylindrical off-body mesh used as background (Figure 20 (a)), and a body-fitted mesh of C-H topology for the blade (Figure 20 (b)). Table 10 lists the grids used and the breakdown of cells per blade. The coarse and medium grids have 6.2 and 9.6 million cells per blade (equivalent to 18.6 and 28.8 million cells for three-bladed rotor, respectively), with the same grid resolution for the body-fitted mesh (3.6 million cells). The background mesh, however, was refined at the wake and near-body regions, increasing the grid size from 2.6 to 6 million

cells. Solutions were obtained with the MUSCL-2 scheme using the coarse and medium grids, whilst the MUSCL-4 was only employed with the coarse grid. Like all chimera cases, the MUSCL-2 and MUSCL-4 schemes were activated at the foreground and background levels, respectively.

Table 10: Mesh size in million cells for the XV-15 rotor mesh.

	Coarse Mesh	**Medium Mesh**
Background mesh size	2.6 million	6.0 million
Blade mesh size	3.6 million	3.6 million
Overall mesh size	6.2 million	9.6 million
Wall distance	$1.0 \times 10^{-5} c_{\text{ref}}$	$1.0 \times 10^{-5} c_{\text{ref}}$

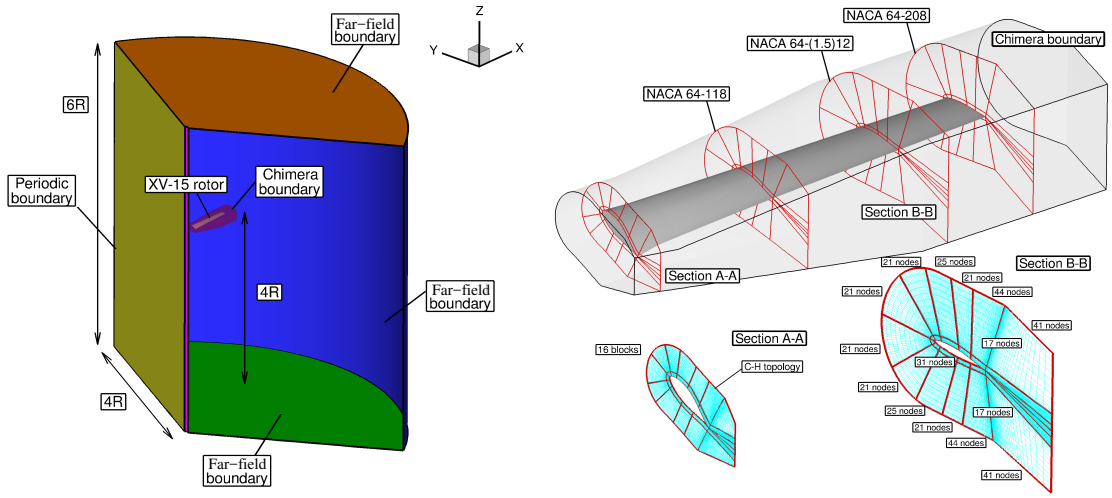

(a) Computational domain.

(b) XV-15 rotor mesh.

Fig. 20: Computational domain and boundary conditions employed (left) and detailed view of the body-fitted XV-15 rotor mesh (right).

Regarding the stability of the MUSCL-4 scheme, Figure 21 shows the residual of the flow solution for the XV-15 tiltrotor blade, with the coarse mesh, as function of the number of iterations for the MUSCL-2 and MUSCL-4 schemes. A similar behaviour is seen between both schemes, with no sign of lack of stability for the MUSCL-4 scheme. This supports the idea that with the introduction of a small amount of dissipation δ, the robustness of the standard HMB solver is maintained when the high-order scheme is used.

Figure 22 shows the effect of the MUSCL-2 and MUSCL-4 schemes on the figure of merit and torque coefficient for the full-scale XV-15 rotor. Experimental data is also shown, carried out by Felker *et al.* [70] at the Outdoor Aeronautic Research Facility (OARF), and by Light [71] and Betzina [69] at the NASA 80×120ft wind tunnel. Vertical lines labelled as empty (4,574 kg, C_T= 0.0073) and maximum gross (6,000 kg, C_T= 0.0096) weight, define the hover range of the XV-15 tiltrotor in hover [72]. Momentum-based estimates of the figure of merit [73] are also included,

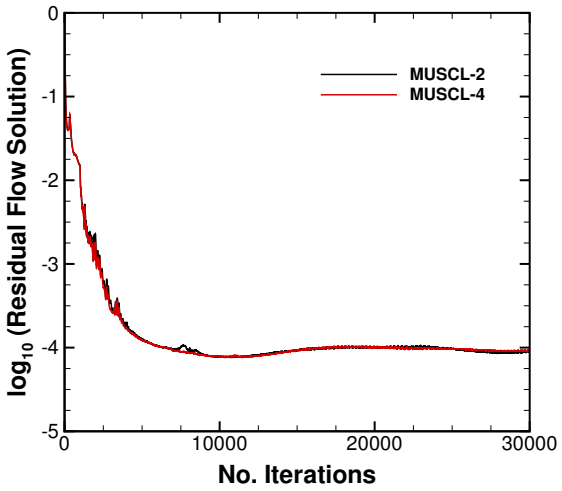

Fig. 21: Residual of the flow solution of the XV-15 tiltrotor blade (coarse mesh) as function of the number of iterations for the MUSCL-2 and MUSCL-4 schemes.

where an induced power factor k_i of 1.1 and overall profile drag coefficient C_{DO} of 0.01 were used. Polynomial fit curves were computed using the obtained CFD results and shown with solid lines and squares (MUSCL-2 with a coarse grid), deltas (MUSCL-2 with a medium grid), and triangles (MUSCL-4 with a coarse grid). The CFD results obtained with the MUSCL-2 scheme are in good agreement with the test data of Betzina [69] for all blade collective angles. Moreover, the grid size has a negligible effect on the overall performance at low thrust, with a small influence at high thrust. Regarding the results obtained with the MUSCL-4 scheme, good agreement is obtained with the MUSCL-2 scheme when using a medium grid, and the experimental data of Betzina.

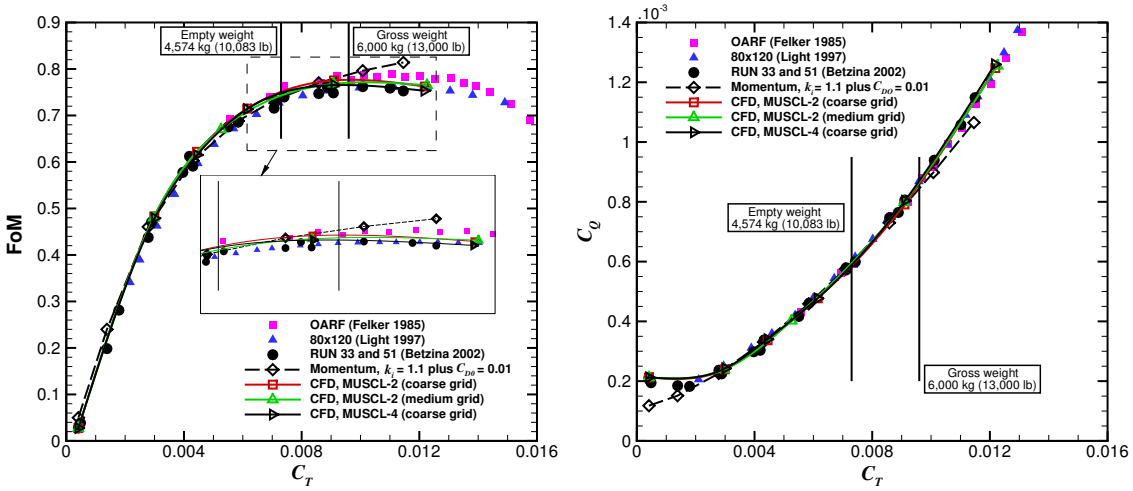

(a) FoM - C_T.

(b) C_Q - C_T.

Fig. 22: Effect of the MUSCL-2 and MUSCL-4 schemes on the figure of merit (left) and torque coefficient (right) for the full-scale XV-15 rotor.

To assess the ability of the MUSCL-4 scheme in accurately predicting loads when a coarse mesh is employed, a comparison between the predicted and measured [74, 75] FoM at a collective angle of 10° is reported in Table 11. Predictions with the MUSCL-2 scheme using coarse and medium grids indicate good correlation with experiments (1.5 and 0.8 counts of FoM, respectively). Results obtained with the MUSCL-4 scheme on a coarse grid present a small discrepancy of 0.5 counts of FoM, which highlights the benefit of using higher-order numerical scheme in accurately predicting integrated airloads.

Table 11: Predicted and experimental [74, 75] figure of merit at collective pitch angle of 10°.

Case	**FoM**	**Difference [%]**
Experiment	0.760	-
MUSCL-2 coarse grid	0.775	1.97%
MUSCL-2 medium grid	0.768	1.05%
MUSCL-4 coarse grid	0.765	0.65%

Despite that the lower-order scheme is sufficient to predict the blade loads [26], it did not preserve the near-blade and wake flow features. In hover, to ensure realistic predictions of the wake-induced effects and therefore induced-drag, the radial and vertical displacements of the vortex core should be resolved, at least for the first and second wake passages.

Figure 23 shows the wake for the full-scale XV-15 rotor using iso-surfaces of $\bar{Q}$-criteria obtained with MUSCL-2 (a) and MUSCL-4 (b) on the same coarse grid of Table 10. It should be mentioned that, a collective pitch angle of 10° degrees was selected for such comparison. It is observed that the MUSCL-4 scheme preserves much better the helical vortex filaments that trail from each of the tip-blade, and the wake sheets trailed along the trailing edge of the blade if compared with the MUSCL-2 solution. Therefore, the lower dissipation of the MUSCL-4 scheme results in an improved preservation of the rotor wake. In this regard, if MUSCL-2 is employed, the vorticity of the vortex cores (computed using the local vorticity maximum criterion) is significantly dissipated at a wake age of $2\pi/3$ (first blade passage in Figure 24) while MUSCL-4 results show a much better wake preservation. Likewise, at wake ages of $4\pi/3$ (second blade passage) and 2π (third blade passage) a reduction of vorticity by 42.8% and 45.2% is observed when MUSCL-2 is employed.

J. CPU and memory overheads

As dicussed earlier, solutions obtained with the MUSCL-4 scheme on the coarse grid show better predicted loads and rotor wake structures. Table 12 reports the computational time, in work units per implicit iteration, for the XV-15 tiltrotor blade when the MUSCL-2 and MUSCL-4 schemes are used with the coarse grid. Solutions were computed on 8 cores of the high performance cluster of Glasgow University Jupiter, comprised of Intel Xeon E5620 3.2 GHz processors. This case shows similar CPU overheads compared to the S-76 and JORP blades, with a penalty of about 16%. CPU

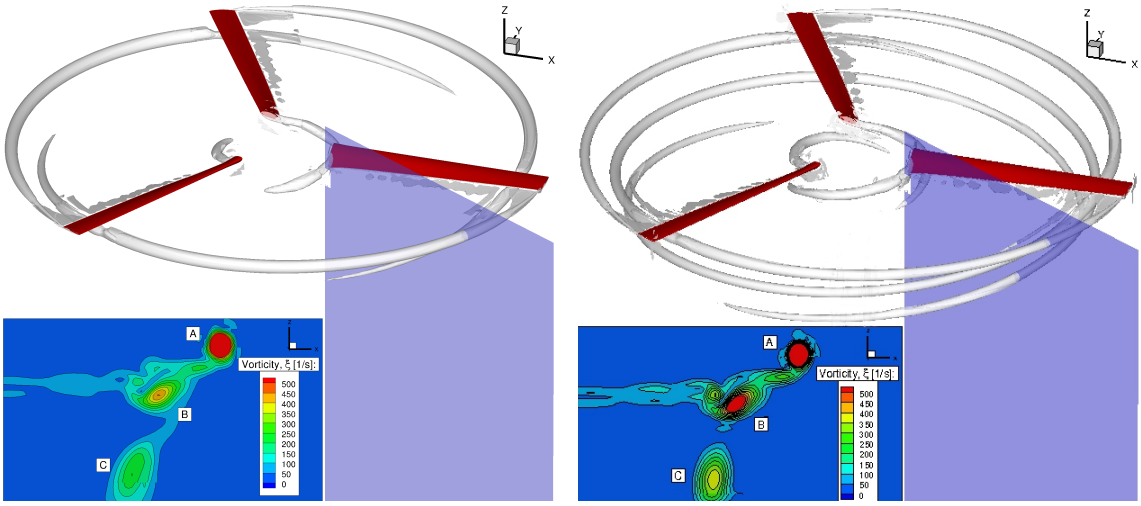

(a) Wake flow using MUSCL-2 scheme.

(b) Wake flow using MUSCL-4 scheme.

Fig. 23: Wake flowfield for the full-scale XV-15 rotor using $\bar{Q}$-criterion ($\bar{Q}$=0.05). Results with the MUSCL-2 (left) and MUSCL-4 (right) schemes.

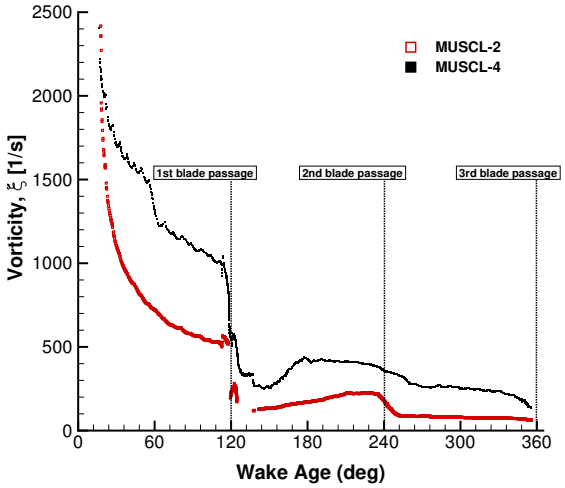

Fig. 24: Vorticity of the tip vortex as function of the wake age in degrees, obtained with the MUSCL-2 and MUSCL-4 schemes on the coarse grid.

overheads of 0.5% and 0.95% are reported for computing the first and second derivatives. Halo data exchanges require 1.71% and 4.4% CPU overheads for the first and second derivatives, respectively, and 6.4% and 2% for computing the new residual Jacobian matrix with the high-order correction terms, and for the solution of the linear system. When comparing solutions with similar errors (see Figure 22 and Table 11), MUSCL-4 scheme on the coarse mesh is 25% less expensive than MUSCL-2 scheme on the medium mesh. Like previous cases, a memory overhead of 23% is added when the MUSCL-4 scheme is used.

Table 12: Computational run-time for the XV-15 tiltrotor blade with MUSCL-2 and MUSCL-4 schemes on the coarse mesh.

Mesh	**Scheme**	**CPU work units/iteration**
Coarse Mesh (6.2 million cells)	MUSCL-2	1
	MUSCL-4	1.16 (16%)
Medium Mesh (9.6 million cells)	MUSCL-2	1.41 (41%)

K. UH-60A rotor in forward flight

To validate the present high-order scheme for three-dimensional unsteady flows with overset and moving grids, the UH-60A rotor in forward flight is also considered. The UH-60A is a four-bladed rotor made of two aerofoil profiles; the SC-1095 and SC-1095R [76]. The planform of the UH-60A rotor features a 20° swept tip covering 6% of the blade radius, with a -16° of non-linear twist. The main geometric characteristics of the UH-60A blade [67, 77, 78] are summarised in Table 13.

Table 13: Geometric properties of the UH-60A rotor [67, 77, 78].

Parameter	**Value**
Number of blades, N_b	4
Rotor radius, R	321.96 inches
Reference blade chord, c_{ref}	20.76 inches
Aspect ratio, R/c_{ref}	15.5
Rotor solidity, σ	0.0821
Non-linear twist, Θ	-16°

The multi-block structured grid for the full rotor has a total of 42.2 million cells with 2,064 blocks, with 42.2 and 8.2 million cells for the background and body-fitted grids, respectively. A hub is also included in the computational domain a modelled as a generic ellipsoidal surface.

The test case selected for validation corresponds to the UH-60A main rotor at high-speed forward flight. Flight test data for this demanding configuration (flight C8534) was acquired by the U.S. Army/NASA UH-60A Airloads Program [79]. The rotor advance ratio was μ= 0.368, and the freestream Mach number was 0.236. To meet the target thrust coefficient (blade loading coefficient C_T/σ= 0.08) while having zero roll and pitch moments, a matrix trimming method is used in HMB [34], which uses the Blade Element Theory (BET) to compute the elements of the sensitivity matrix. The flow solutions corresponding to the MUSCL-2 and MUSCL-4 schemes were computed solving the URANS equations, coupled with Menter's k-ω SST turbulence model [55]. The employed time step corresponds to 0.25 deg in the azimuthal direction and was based on experience gained with previous rotor computations in forward flight [33]. The trim state is specified in Table 14 and the comparison of the blade normal force and pitch moment (with mean value removed) at three radial

stations is shown in Figure 25. Good agreement is seen between experimental data and predicted loads with similar trends observed between the MUSCL-2 and MUSCL-4 results.

Table 14: Trim state for the UH-60A forward flight case using MUSCL-2 and MUSCL-4 schemes.

Parameter	**Value**	
	MUSCL-2	MUSCL-4
μ	0.368	0.368
M_{tip}	0.648	0.648
θ_{shaft}	7.30°	7.30°
θ_0	12.13°	11.97°
θ_{1s}	8.58°	8.35°
θ_{1c}	−2.27°	−2.17°
β_0	3.43°	3.43°
β_{1s}	−1.0°	−1.0°
β_{1c}	−0.70°	−0.70°

Visualisation of the UH-60A rotor flowfield using the $\bar{Q}$-criterion [80] is presented in Figure 26 for the MUSCL-2 and MUSCL-4 approaches. The wake obtained with MUSCL-4 is preserved better than the one obtained with MUSCL-2. Three radial stations are selected for comparisons. Figures 27 and 28 show vorticity contours at planes x/R= 0.5 and 1, respectively, of blade 1 (ψ= 0). Results with MUSCL-4 show a higher resolution of the rotor wake structures at the advancing and retreating rotor disk sides if compared with MUSCL-2. In fact, vortex C ($\psi = 270°$) computed with MUSCL-2 in Figures 27 and 28 show a reduction of the core vorticity by almost 20% respect to the MUSCL-4 results. Figure 29 shows vorticity contours at the plane x/R= 2 (dashed lines in Figure 26), which highlight the capacity of the MUSCL-4 scheme in preserving the vortex cores and rotor wake structures (A, and B in Figure 29).

L. CPU and memory overheads

Table 15 reports the computational run-time in work units per implicit iteration for the UH-60A rotor in forward flight when MUSCL-2 and MUSCL-4 schemes are used on the same grid. The multi-block structured grid for this case has a total of 39.3 million cells with 2,064 blocks, with 31.1 and 8.2 million cells for the background and body-fitted grids, respectively. Due to the large size, this case needs to be computed in parallel mode, so solutions employed 48 cores of the high performance cluster of Glasgow University Jupiter. For the S-76, JORP propeller, and XV-15 blades, results with MUSCL-4 show CPU penalties of 22%, 13%, and 16%, respectively, where the computational cost associated with the halo data of the first and second derivatives is less than 5%. This is not the case when larger meshes are used, mainly due to the amount of data exchange between processors. A CPU overhead of about 130% is added for MUSCL-4 if used for the UH-60A rotor in forward flight. CPU overheads of 0.69% and 1.52% are required for computing the first

and second derivatives and 39.95% and 79.98% for the halo data exchanges for the first and second derivatives, respectively. This calls for better parallelisation of the scheme in order to reduce the CPU overheads. Regarding memory overheads, 23% is added when the MUSCL-4 scheme is used.

Table 15: Computational run-time for the UH-60A rotor in forward flight with MUSCL-2 and MUSCL-4 schemes on the same mesh.

Mesh	**Scheme**	**CPU work units/iteration**
39.3 million cells mesh	MUSCL-2	1
	MUSCL-4	2.3 (130%)

M. ERICA tiltrotor in aeroplane mode

To demonstrate the current scheme for complex cases, a complete tiltrotor is simulated. Numerical simulations of the ERICA aircraft using the MUSCL-2 and MUSCL-4 schemes were performed and results are presented here. The ERICA tiltrotor is a tiltwing aircraft, where an outboard part of the wing can be partially rotated to mitigate the strong aerodynamic interaction between rotor and wing and to reduce the downward force acting on the wings in hover. In this regard, the research project NICETRIP [81] (Novel Innovative Competitive Effective Tilt Rotor Integrated Project) was funded by the European Union (EU) to develop a database covering aerodynamic interactional phenomena and other technology aspects of tiltwing vehicles. In this framework, a 1:5 motorised model-scale tiltrotor was designed and manufactured under the name of ERICA (Enhanced Rotorcraft Innovative Concept Achievement) [82] and experiments were undertaken using the 9.5×9.5m DNW-LLF (German-Dutch Wind Tunnels Large Low-speed Facility) and the 8m S1MA ONERA wind tunnels. For this study, an aeroplane configuration was selected, where the rotor blades were fully resolved.

The chimera method was employed to ease mesh generation. Self-contained component grids for the main fuselage and the nacelle-tiltable wing were built, while four ADYN blades were embedded in the nacelle mesh component. A Cartesian off-body mesh was used as background to capture the convection of the tip vortex generated by the blades. Table 16 compares the mesh size used here for CFD computation. The multi-block overset arrangement of the ERICA tiltrotor for an aeroplane mode case is shown in Figure 30.

Table 17 summarises the employed test conditions. The aeroplane mode is labelled AC1 (Aeroplane Configuration 1), and refers to a very low speed aeroplane-mode M_∞= 0.168, along with a large aircraft AoA of δ_{FU}= 10.02 degrees. Neither the nacelles nor the tiltable wings were tilted with respect to the fuselage (δ_{FU}= δ_{NAC}= δ_{TW}). The Reynolds numbers, based on the reference length L_{ref} and on the freestream velocity V_∞, was 1.70×10^6.

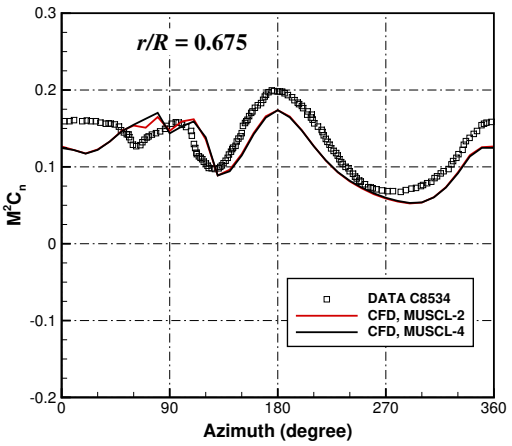

(a) r/R= 0.675.

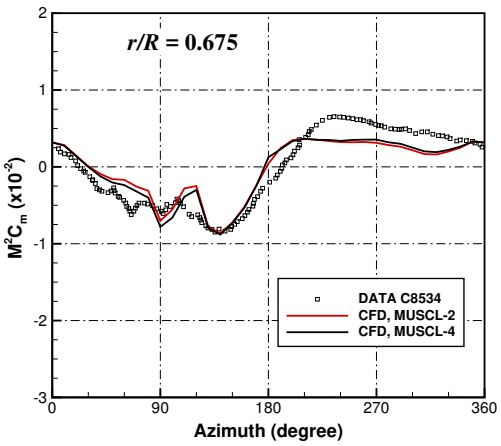

(b) r/R= 0.675.

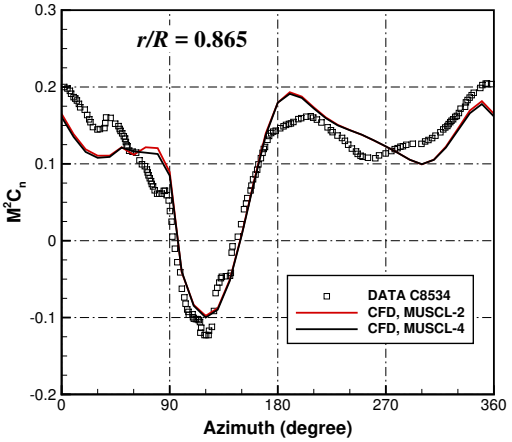

(c) r/R= 0.865.

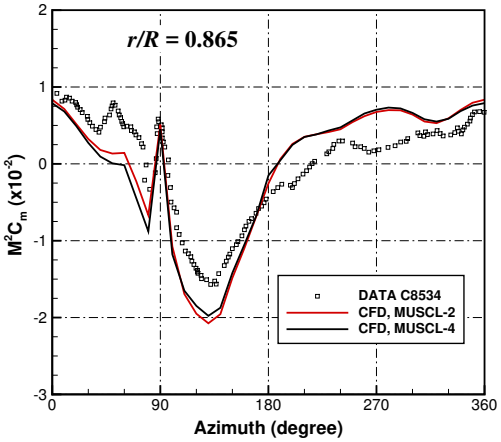

(d) r/R= 0.865.

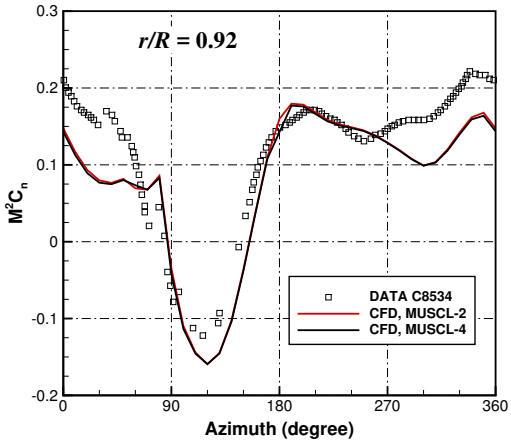

(e) r/R= 0.92.

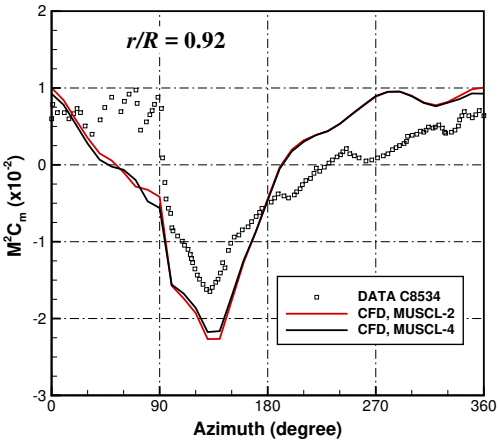

(f) r/R= 0.92.

Fig. 25: Comparison between experimental data and predictions using MUSCL-2 and MUSCL-4 schemes for the UH-60A blade normal force and pitch moment (with mean value removed) at advance ratio (μ= 0.368) at three radial stations.

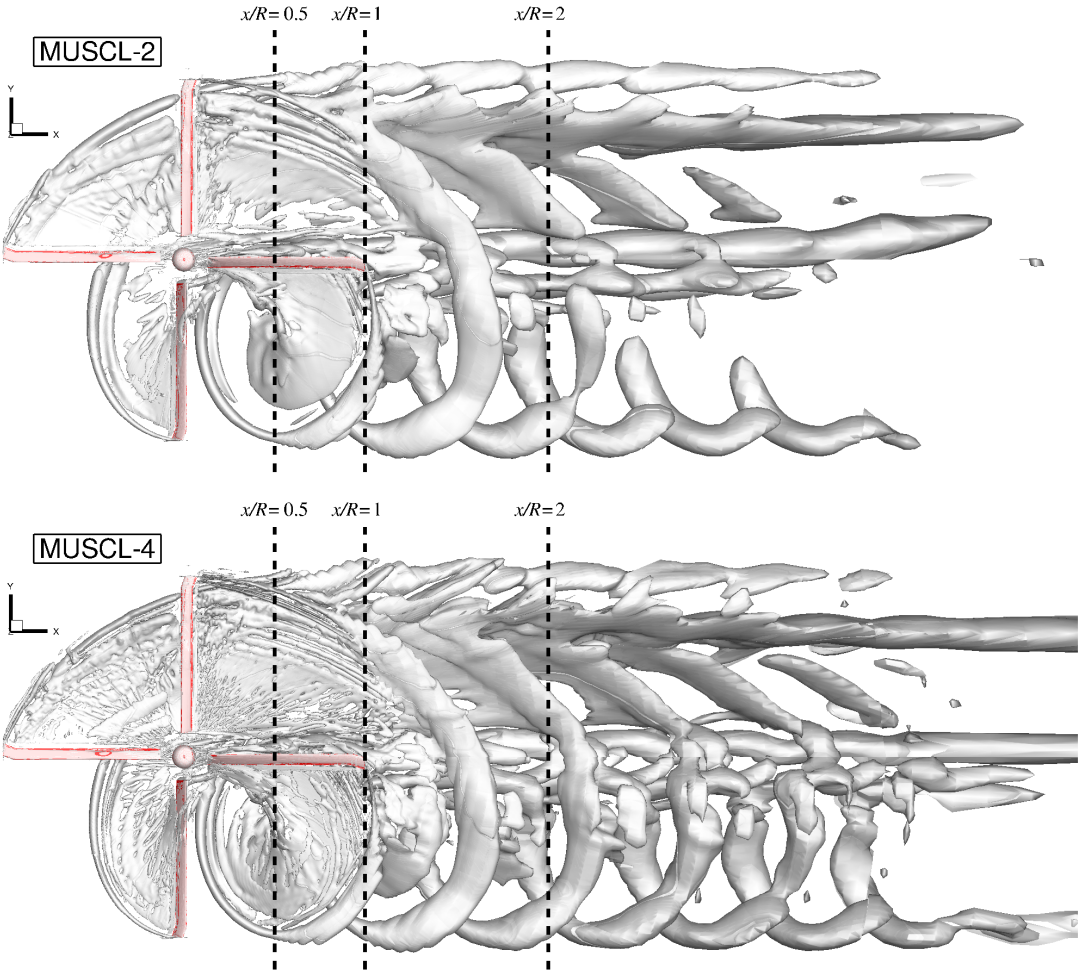

Fig. 26: Wake-visualisation of the UH-60A rotor in forward flight using $\bar{Q}$-criterion ($\bar{Q}$=0.0007). Results with the MUSCL-2 (top) and MUSCL-4 (bottom) schemes.

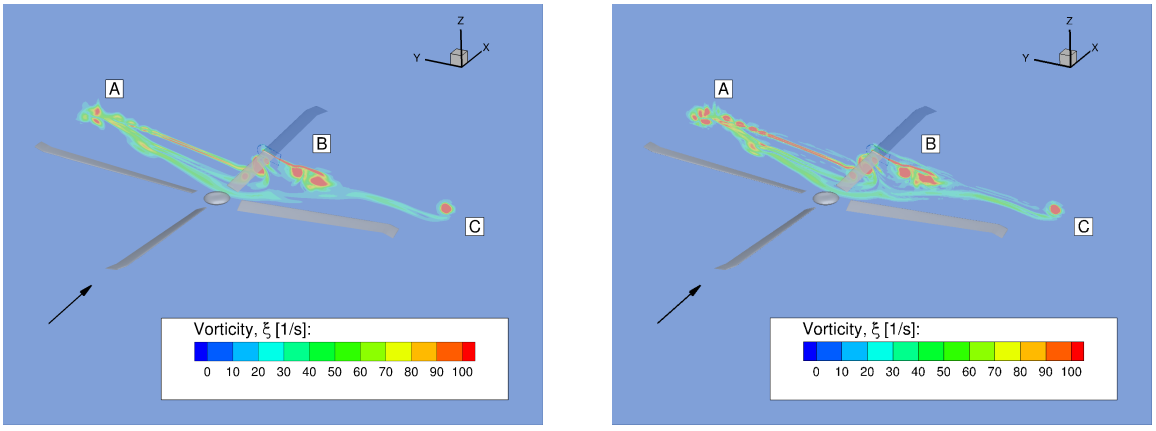

(a) MUSCL-2 scheme.

(b) MUSCL-4 scheme.

Fig. 27: Vorticity contours at the plane x/R= 0.5 of the blade 1 (ψ= 0) for the MUSCL-2 and MUSCL-4 schemes.

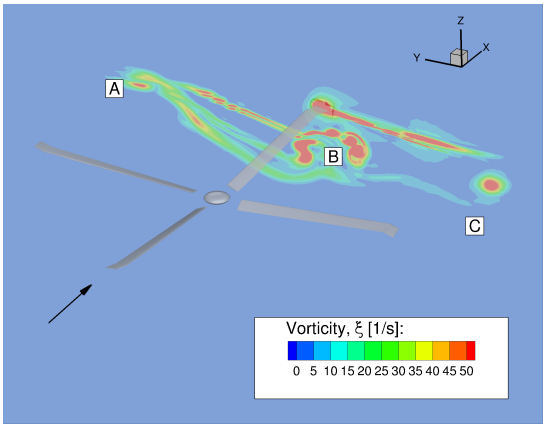

(a) MUSCL-2 scheme.

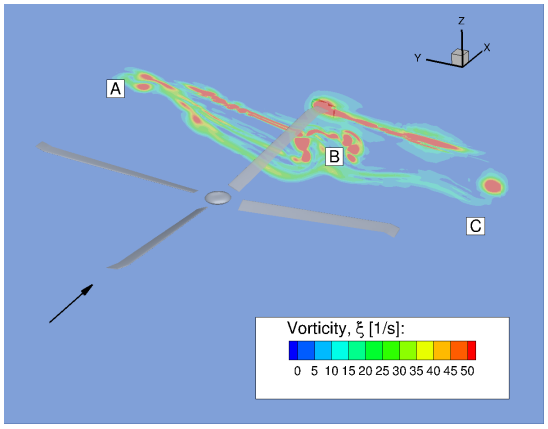

(b) MUSCL-4 scheme.

Fig. 28: Vorticity contours at the plane x/R= 1 of the blade 1 (ψ= 0) for the MUSCL-2 and MUSCL-4 schemes.

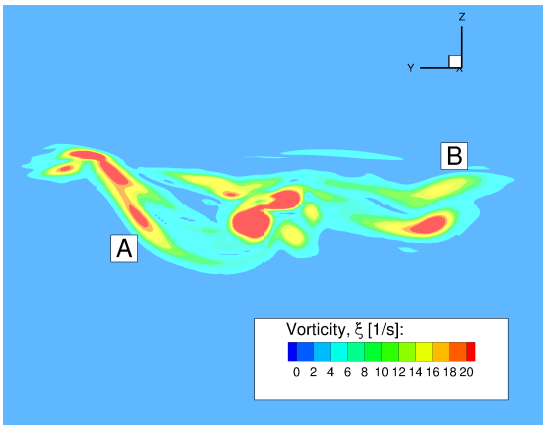

(a) MUSCL-2 scheme.

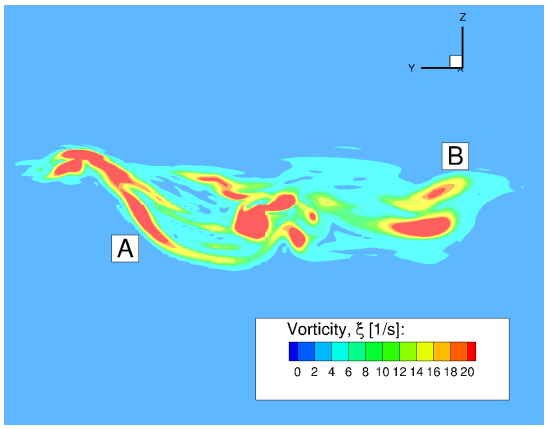

(b) MUSCL-4 scheme.

Fig. 29: Vorticity contours at the plane x/R= 2 of the blade 1 (ψ= 0) for the MUSCL-2 and MUSCL-4 schemes.

Table 16: ERICA model-scale component mesh sizes, given as million nodes.

Components	**Aeroplane Mode**
Fuselage and fixed wing	9.9
Nacelle and tiltable wing	30.3
Rotor blades (x4)	11.4
Wind tunnel	4.6
Total	**56.2**

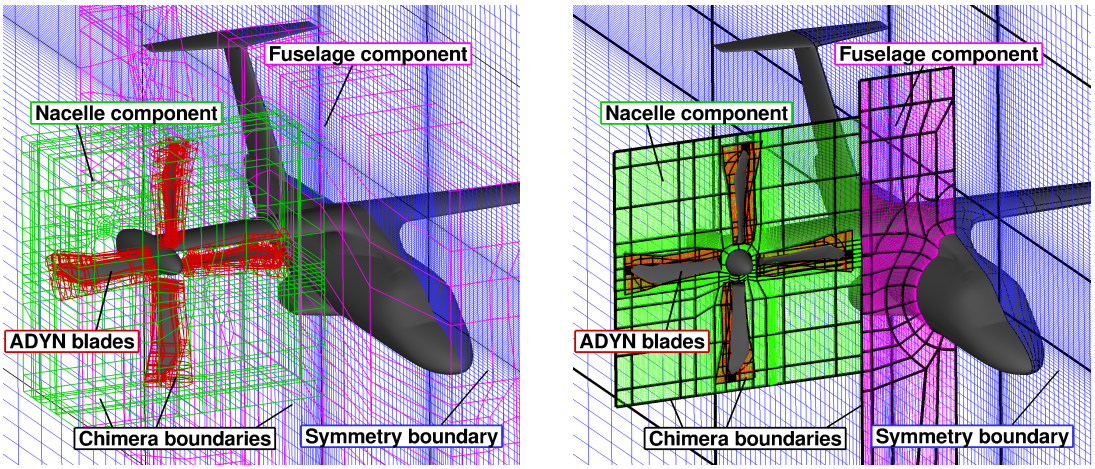

(a) Multi-block grid.

(b) Cross section of the multi-block grid.

Fig. 30: Details of the multi-block overset arrangement of the ERICA tiltrotor in aeroplane mode configuration. Blue line=background component; Purple line=fuselage component; Green line= nacelle component; Grey line=blade component.

Table 17: Test conditions for the aeroplane mode AC1 [83, 84].

Parameters	**Aeroplane Mode AC1**
M_∞	0.168
M_{tip}	0.470
$\mu = M_\infty / M_{\text{tip}}$	0.357
Re_{ref}	1.70×10^6
δ_{FU} [deg]	10.02°
δ_{NAC} [deg]	10.02°
δ_{TW} [deg]	10.02°
RPM blade rotor	2130
θ_{75} [deg]	27.36°

Eight cross-sections were selected for C_P profile comparisons between CFD and experiments [85, 86] (see Table 18). One section was selected on the top symmetry planes of the fuselage (labelled with SYM-TOP), one section on the fixed wing (labelled with FW), two on the tiltable wing (labelled with TW) that define the zone of aerodynamic interaction between the tiltable wing and the blades, and four on the fuselage (labelled with FU). Figure 31 shows the position of the selected sections on the ERICA tiltrotor for the aeroplane mode AC1.

Table 18: Nomenclature of the stations selected for C_P profile comparisons. FU=Fuselage; FW=Fixed Wing; TW=Tiltable Wing; SYM=Symmetry.

Nomenclature	**Description**
SYM-TOP	Fuselage symmetry plane (top), station y=0 mm.
FW-A	Fixed wing, station y=490 mm.
TW-A	Tiltable wing, station y=855 mm.
TW-B	Tiltable wing, station y=1117.5 mm.
FU-A	Fuselage, station x=260 mm.
FU-B	Fuselage, station x=1163 mm.
FU-C	Fuselage, station x=1810 mm.
FU-D	Fuselage, station x=2760 mm.

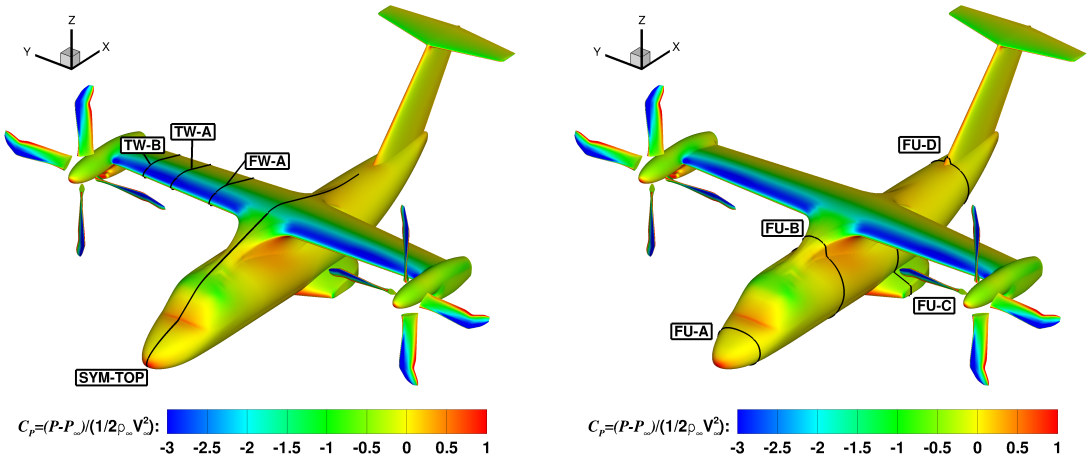

(a) Sections on the fixed and tiltable wings.

(b) Sections on the fuselage.

Fig. 31: Cross-sections selected for comparisons between CFD and experiments [85, 86] on the fixed and tiltable wings, and fuselage of the ERICA tiltrotor for the aeroplane mode configuration. MUSCL-2 solution.

C_P profile comparisons between CFD and experiments [85, 86] on the fuselage, fixed and tiltable wings of the ERICA tiltrotor are given in Figure 32. They correspond to the top fuselage centre-line and inner, middle, and outer tiltable and fixed wing sections. The CFD results were not averaged in phase, which could lead to a source of error in comparisons, since all test data is phase averaged.

For both cases, C_P values were averaged over the last computed rotor revolution. Regarding the C_P profile at the centre-line of the fuselage (Figure 32 (a)), a zone of recirculation is seen in both sets of experiments (Modane and DNW experiments are denoted by squares and triangles, respectively) represented by a pressure plateau after the wing leading edge suction peak. The HMB predictions (MUSCL-2=red line, MUSCL-4=green line) overestimate the suction peak and do not capture the region of recirculation. This can be due to a failure of the employed turbulence model, wind tunnel effects, and lack of the exact trim state used during the tunnel tests.

In the middle fixed and tiltable wing sections (Figures 32 (c) and 32 (d)), wind tunnel experiments show good agreement, with small differences of 9% for the suction peak. Note that the differences between the two sets of experiments are always larger than the differences between the MUSCL-2 and MUSCL-4 results.

Figure 33 presents C_P comparisons on the ERICA fuselage at four cross-sections. As can been seen, all CFD curves are close to the experimental data. Better agreement is obtained at the front of the fuselage, where the flow is attached. Both solutions capture well all features shown by the experiments. Even for stations located behind the fixed wing, the agreement is still fair near the sponsons and the fin of the model.

Regarding the MUSCL-2 solution, the wake behind the rotor disk (see Figure 34a) is preserved for more than one rotor diameter downstream. This informative plot shows the interaction of the rotor wake with the nacelle and tiltable wings. From these iso-surfaces it can be seen that the rotor wake does not directly interact with the fuselage and the fixed part of the wings. Iso-surface contours of $\bar{Q}$-criterion are also shown for the MUSCL-4 scheme in Figure 34b. The Figure reveals that the detailed wake characteristics can be easily identified when using high-order schemes.

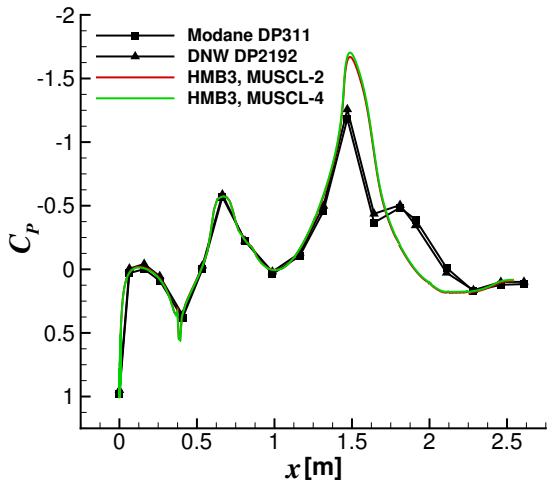

(a) SYM-TOP, section y=0 mm.

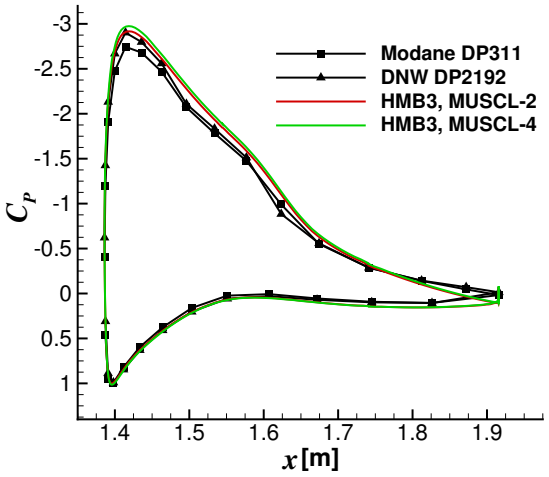

(b) FW-A, section y=490 mm.

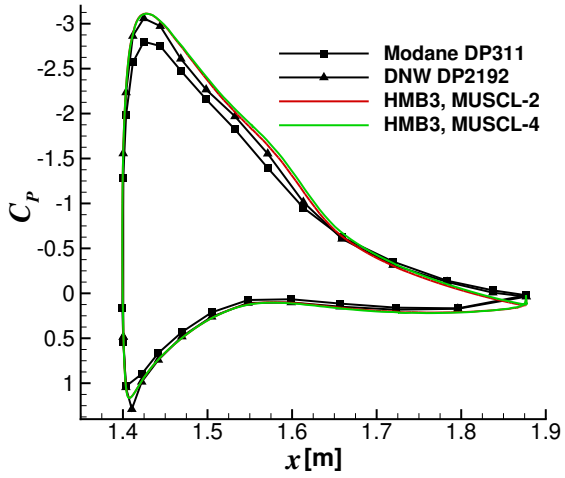

(c) TW-A, section y=855 mm.

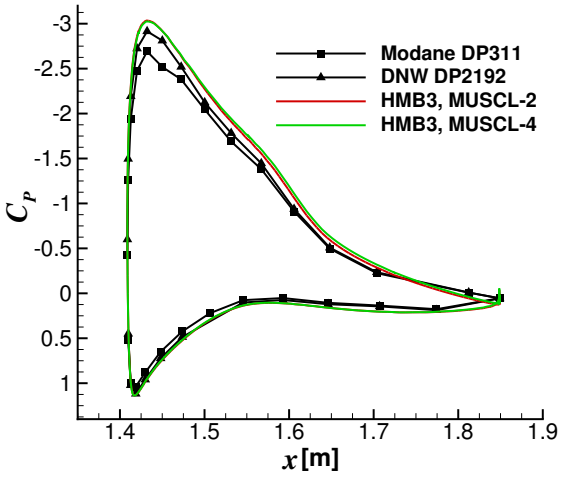

(d) TW-B, section y=1117.5 mm.

Fig. 32: C_P profile comparisons between CFD and experiments [85, 86] on the fixed and tiltable wings of the ERICA tiltrotor for the aeroplane mode configuration AC1.

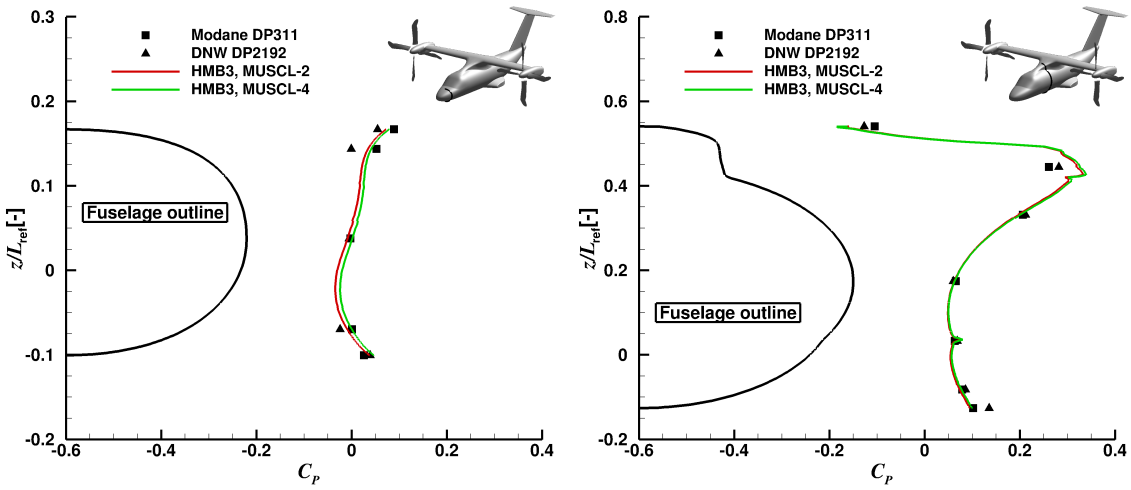

(a) FU-A, section x=260 mm.

(b) FU-B, section x=1163 mm.

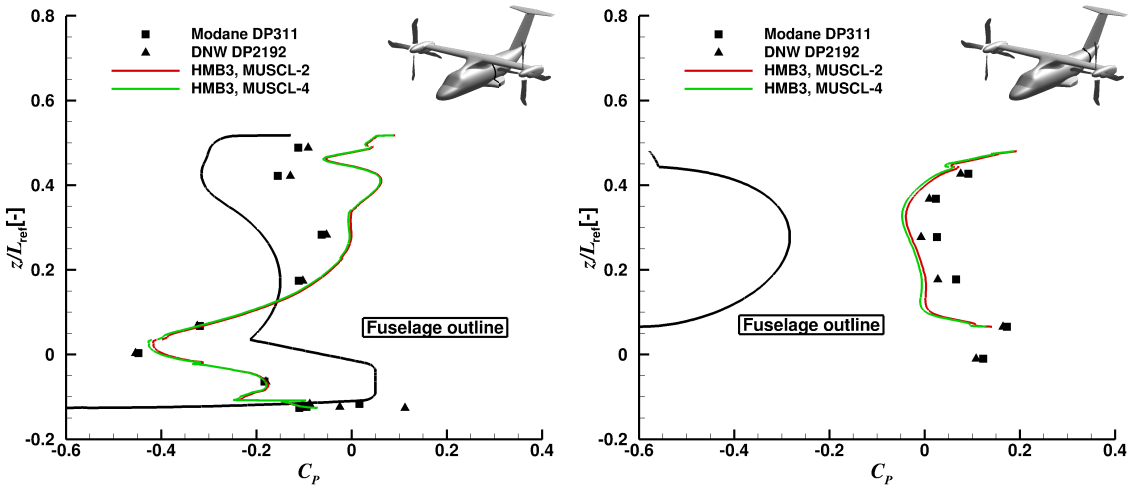

(c) FU-C, section x=1810 mm.

(d) FU-D, section x=2760 mm.

Fig. 33: C_P profile comparisons between CFD and experiments [85, 86] on the fuselage of the ERICA tiltrotor for the aeroplane mode configuration AC1.

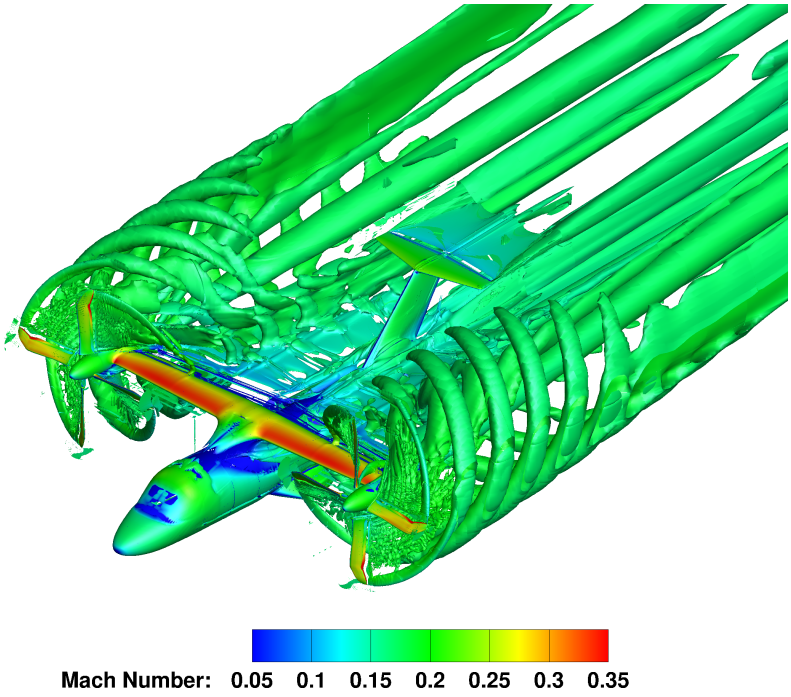

(a) Wake of the MUSCL-2 solution.

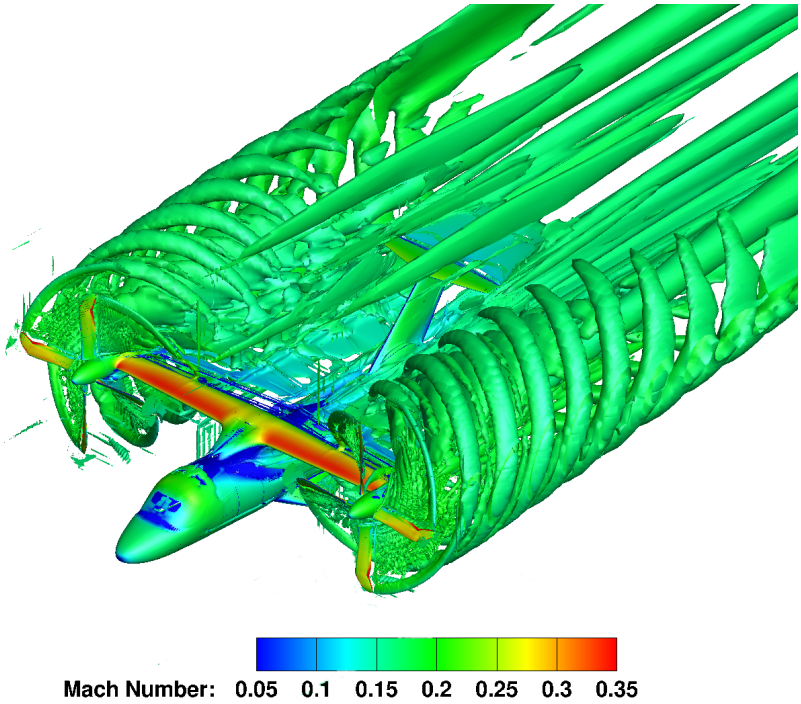

(b) Wake of the MUSCL-4 solution.

Fig. 34: Wake-visualisation of the ERICA tiltrotor in aeroplane mode configuration using $\bar{Q}$-criterion ($\bar{Q}$=0.007) shaded by contour of Mach numbers. Results with the MUSCL-2 (top) and MUSCL-4 (bottom) schemes.

N. CPU and memory overheads

Table 19 reports the run-time in work units per implicit iteration for the ERICA tiltrotor with the MUSCL-2 and MUSCL-4 schemes are used on the same grid. Solutions were computed on 48 cores of the high performance cluster of Glasgow University Jupiter, comprised of Intel Xeon E5620 3.2 GHz processors. As seen with the UH-60A rotor in forward flight, a penalty is paid when the halo data of the first and second derivatives are exchanged for parallel execution. So, this case shows CPU overheads of 144%. CPU overheads of 0.13% and 0.26% are reported to compute first and second derivatives, showing a small penalty of 0.39%. However, halo data exchanges require 48.2% and 96.31% for the first and second derivatives, respectively. Despite their promising results obtained with MUSCL-4 showing the ability of the scheme in preserving much better the wake, a more efficient parallelisation of the halo exchange data is needed for grids of more than 10 million cells.

Table 19: Computational run-time for the ERICA tiltrotor with MUSCL-2 and MUSCL-4 schemes on the same mesh.

Mesh	**Scheme**	**CPU work units/iteration**
56.2 million cells mesh	MUSCL-2	1
	MUSCL-4	2.44 (144%)

IV. Summary and Future Work

The implementation of a high-order, finite-volume scheme in the HMB CFD solver has been presented. The scheme showed a higher level of accuracy if compared with the standard-MUSCL extrapolation, and 4th-order accuracy was achieved on Cartesian grids. Furthermore, a significantly higher spectral resolution (dispersion and dissipation) of the new scheme is observed. Two-and three-dimensional test cases have been considered to demonstrate the new formulation. Results of the steady flow around the 7AD, the S-76 helicopter rotor, the JORP propeller, and the XV-15 tiltrotor blades showed a better wake and higher resolution of the vortical structures compared with the standard MUSCL solution, with a small CPU and memory overhead. The method was also demonstrated for three-dimensional unsteady flows using overset and moving grid computations for the UH-60A rotor in forward flight and the ERICA tiltrotor in aeroplane mode. However, the computational expense associated to the parallelisation of the halo data exchange between processors for the first and second derivate make this scheme not efficient for large meshes (above 50 million cells). Nevertheless, the method shows promising results in capturing and preserving the rotor wake along with small penalty in terms of CPU and memory if compared with MUSCL-2 scheme for medium grid size (up to 10 million cells). We believe that similar penalties can be obtained for larger grids with a modification of the data exchange process in parallel.

Based on the aforementioned conclusions, the following future steps are suggested:the halo data exchanges for the first and second derivatives need to be optimised to lower CPU overheads for the investigated MUSCL-4 scheme and the use of this scheme combined with LES techniques will be used to evaluate far wake encounters.

V. Acknowledgments

The use of the cluster Jupiter of the University of Glasgow is gratefully acknowledged. Part of this work is funded under the HiperTilt Project of the UK Technology Strategy Board (TSB) and Leonardo Helicopters under Contract Nr. 101370.

[1] Liu, Y., Anusonti-Inthra, P., and Diskin, B., "Development and Validation of a Multidisciplinary Tool for Accurate and Efficient Rotorcraft Noise Prediction," NASA CR–2011-217057, Feb. 2011.

[2] Wang, Z. J., Fidkowski, K., Abgrall, R., Bassi, F., Caraeni, D., Cary, A., Deconinck, H., Hartmannn, R., Hillewaert, K., Huynh, H. T., Kroll, N., May, G., Persson, P.-O., van Leer, B., and Visbal, M., "High-Order CFD Methods: Current Status and Perspective," *International Journal for Numerical Methods in Fluids*, Vol. 72, No. 8, 2013, pp. 811–845, doi: 0.1002/fld.3767.

[3] Kroll, N., Bieler, H., Deconinck, H., Couaillier, V., van der Ven, H., and Sorensen, K., "ADIGMA - a European Initiative on the Development of Adaptive Higher-Order Variational Methods for Aerospace Applications," *Notes on Numerical Fluid Mechanics and Multidisciplinary Design*, Vol. 113, 2010.

[4] Jimenez-Garcia, A. and Barakos, G. N., "Accurate Predictions of Rotor Hover Performance at Low and High Disc Loadings," *Journal of Aircraft, Advance online publication*, 2017, doi: 10.2514/1.C034144.

[5] Gottlieb, S. and Orszag, A., *Numerical Analysis of Spectral Methods: Theory and Applications*, SIAM: Philadelphia, 1977.

[6] Godunov, S. K., "A Finite-Difference Method for the Numerical Computation of Discontinuous Solutions of the Equations of Fluid Dynamics," *Matematicheski Sbornik*, Vol. 47, No. 3, 1959, pp. 271–306.

[7] Lele, S. K., "Compact Finite Difference Schemes with Spectral-like Resolution," *Journal of Computational Physics*, Vol. 103, No. 1, 1992, pp. 16–42, doi: 10.1016/0021-9991(92)90324-R.

[8] Liu, X., Osher, S., and Chan, T., "Weighted Essentially Non-Oscillatory Schemes," *Journal of Computational Physics*, Vol. 115, No. 1, 1994, pp. 200–212, doi: 10.1006/jcph.1994.1187.

[9] Barth, T. and Frederickson, P., "High-order Solution of the Euler Equations on Unstructured Grids Using Quadratic Reconstruction," *AIAA Journal*, Vol. 90, No. 13, 1990, doi: 10.2514/6.1990-13.

[10] Nogueira, X., Colominas, I., Cueto-Felgueroso, L., Khelladi, S., Navarrina, F., and Casteleiro, M., "Resolution of Computational Aeroacoustics Problems on Unstructured Grids with a Higher-Order Finite Volume Scheme," *Journal of Computational and Applied Mathematics*, Vol. 234, No. 7, 2010, pp. 2089–2097, doi: 10.1016/j.cam.2009.08.067.

[11] Yang, H. Q., Chen, Z. J., Przekwas, A., and Dudley, J., "A High-Order CFD Method Using Successive Differentiation," *Journal of Computational Physics*, Vol. 281, No. 1, 2015, pp. 690–707, doi: 10.1016/j.jcp.2014.10.046.

[12] Yang, H. Q. and Harris, R. E., "Vertex-Centered, High-order Schemes for Turbulent Flows," *Proceedings of the 54th Aerospace Sciences Meeting*, San Diego, California, USA, AIAA-2016-1098, 2016, pp. 1–24.

[13] Tam, C. K. W. and Webb, J. C., "Dispersion-Relation-Preserving Finite Difference Schemes for Computational Acoustics," *Journal of Computational Physics*, Vol. 107, No. 2, 1993, pp. 262–281, doi:

10.1006/jcph.1993.1142.

[14] Visbal, M. R. and Gaitonde, D. V., "High-Order Accurate Methods for Complex Unsteady Subsonic Flows," *AIAA Journal*, Vol. 37, No. 10, 1999, pp. 1231–1239, doi: 10.2514/2.591.

[15] McCorquodale, P. and Colella, P., "A High-Order Finite-Volume Method for Conservation Laws on Locally Refined Grids," *Communications in Applied Mathematics and Computational Science*, Vol. 6, No. 1, 2011, pp. 1–25, doi: 10.2140/camcos.2011.6.1.

[16] Colella, P., Dorr, M. R., Hittinger, J. A. F., and Martin, D. F., "High-Order, Finite-Volume Methods in Mapped Coordinates," *Journal of Computational Physics*, Vol. 230, No. 8, 2011, pp. 2952–2976, doi: 10.1016/j.jcp.2010.12.044.

[17] Ekaterinaris, J. A., "High-order accurate, low numerical diffusion methods for aerodynamics," *Progress in Aerospace Sciences*, Vol. 41, No. 1, 2005, pp. 192–300, doi: 10.1016/j.paerosci.2005.03.003.

[18] Calhoun, D. A., Helzel, C., and Leveque, R. J., "Logically Rectangular Grids and Finite Volume Methods for PDEs in Circular and Spherical Domains," *SIAM Rev.*, Vol. 50, No. 4, 2008, pp. 723–752, doi: 10.1137/060664094.

[19] Harten, A., Engquist, B., Osher, S., and Chakravarthy, S., "Uniformly High Order Essentially Non-Oscillatory Schemes, III," *Journal Computational Physics*, Vol. 131, No. 1, 1997, pp. 3–47, doi: 10.1006/jcph.1996.5632.

[20] Shu, C.-W. and Osher, S., "Efficient Implementation of Essentially Non-Oscillatory Shock Capturing Schemes," *Journal Computational Physics*, Vol. 77, No. 2, 1988, pp. 439–471, doi: 10.1016/0021-9991(88)90177-5.

[21] Shu, C.-W. and Osher, S., "Efficient Implementation of Essentially Non-Oscillatory Shock Capturing Schemes, II," *Journal Computational Physics*, Vol. 83, No. 1, 1989, pp. 32–78, doi: 10.1016/0021-9991(89)90222-2.

[22] Jiang, G. and Shu, C.-W., "Efficient Implementation of Weighted ENO Schemes," *Journal of Computational Physics*, Vol. 126, No. 1, 1996, pp. 202–228, doi: 10.1006/jcph.1996.0130.

[23] Balsara, D. and Shu, C.-W., "Monotonicity Preserving Weighted Essentially Non-Oscillatory Schmes with Increasingly High Order of Accuracy," *Journal Computational Physics*, Vol. 160, No. 2, 2000, pp. 405–452, doi: 10.1006/jcph.2000.6443.

[24] Levy, D., Puppo, G., and Russo, G., "Central WENO Schemes for Hyperbolic Systmes of Conservation Laws," *Mathematical Modelling and Numerical Analysis*, Vol. 33, No. 3, 1999, pp. 547–571, doi: 10.1051/m2an:1999152.

[25] Levy, D., Puppo, G., and Russo, G., "Central WENO Schemes for Hyperbolic Systmes of Conservation Laws," *SIAM Journal on Scientific Computing*, Vol. 22, No. 2, 2000, pp. 656–672, doi: 10.1137/S1064827599359461.

[26] Ghosh, D., *Compact-Reconstruction Weighted Essentially Non-Oscillatory Schemes for Hyperbolic Conservation Laws*, Ph.D. thesis, University of Maryland, United States, Jan. 2013.

[27] Shu, C.-W., "Essentially Non-Oscillatory and Weighted Essentially Non-Oscillatory Schemes for Hyperbolic Conservation Laws, in Advanced Numerical Approximation of Nonlinear Hyperbolic Equations," *Lecture Notes in Mathematics, Springer*, Vol. 1697, No. 1, 1998, pp. 325–432, doi: 10.1007/BFb0096355.

[28] Yeshala, N., Egolf, T., Vasilescu, R., and Sankar, L., "Application of Higher Order Spatially Accurate Schemes to Rotors in Hover," *Proceeding of the 24th Applied Aerodynamics Conference*, San Francisco, California, AIAA 2006-2818, 2006, pp. 1–13.

[29] Hariharan, N., "High Order Accurate Numerical Convection of Vortices Across Overset Interfaces," *Proceedings of the 43rd Aerospace Sciences Meeting*, Reno, Nevada, AIAA 2005-1263, 2005, pp. 1–29.

[30] Xu, L. and Weng, P., "High Order Accurate and Low Dissipation Method for Unsteady Compressible Viscous Flow Computation on Helicopter Rotor in Forward Flight," *Journal of Computational Physics*, Vol. 258, No. 1, 2014, pp. 470–488, doi: 10.1016/j.jcp.2013.10.033.

[31] Barakos, G., Steijl, R., Badcock, K., and Brocklehurst, A., "Development of CFD Capability for Full Helicopter Engineering Analysis," *Proceedings of the 31st European Rotorcraft Forum*, ERF, Florence, Italy, 2005, pp. 1–15.

[32] Lawson, S. J., Steijl, R., Woodgate, M., and Barakos, G. N., "High performance computing for challenging problems in computational fluid dynamics," *Progress in Aerospace Sciences*, Vol. 52, 2012, pp. 19–29, doi: 10.1016/j.paerosci.2012.03.004.

[33] Steijl, R. and Barakos, G. N., "Sliding mesh algorithm for CFD analysis of helicopter rotor-fuselage aerodynamics," *International Journal for Numerical Methods in Fluids*, Vol. 58, No. 5, 2008, pp. 527–549, doi: 10.1002/d.1757.

[34] Steijl, R., Barakos, G. N., and Badcock, K., "A Framework for CFD Analysis of Helicopter Rotors in Hover and Forward Flight," *International Journal for Numerical Methods in Fluids*, Vol. 51, No. 8, 2006, pp. 819–847, doi: 10.1002/fld.1086.

[35] Baverstock, K., "AugustaWestland's Application of HMB to Simulate the Active Gurney Flap," *Proceeding of the 40th European Rotorcraft Forum*, Southampton, UK, ERF-2014-097, 2014, pp. 1–16.

[36] Burg, C. O. E., "Higher Order Variable Extrapolation For Unstructured Finite Volume RANS Flow Solvers," *Proceedings of the Seventieth AIAA Computational Fluid Dynamics Conference*, AIAA, Toronto, Ontario, 2005, pp. 1–17.

[37] van Leer, B., "Towards the Ultimate Conservative Difference Scheme. V. A Second-Order Sequel to Godunov's Method," *Journal of Computational Physics*, Vol. 32, No. 1, 1979, pp. 101–136, doi: 10.1016/0021-9991(79)90145-1.

[38] Anderson, W. K., Thomas, J. L., and van Leer, B., "Comparison of Finite Volume Flux Vector Splittings for the Euler Equations," *AIAA Journal*, Vol. 24, No. 9, 1986, pp. 1453–1460, doi: 10.2514/3.9465.

[39] Mavriplis, D. J., "Revisiting the Least-Squares Procedure for Gradient Reconstruction on Unstructured Meshes," *Proceedings of the 16th Computational Fluid Dynamics Conference*, Orlando, Florida, USA, AIAA-2003-3986, 2003, pp. 1–13.

[40] van Albada, G. D., van Leer, B., and Roberts, W. W., "A Comparative Study of Computational Methods in Cosmic Gas Dynamics," *Astronomy and Astrophysics*, Vol. 108, No. 1, 1982, pp. 76–84.

[41] Michalak, K., "Limiters for Unstructured Higher-Order Accurate Solutions of the Euler Equations," *Proceedings of the 44th Aerospace Sciences Meeting and Exhibit*, Reno, Nevada, USA, AIAA-2008-776, 2008, pp. 1–14.

[42] Jimenez-Garcia, A. and Barakos, G. N., "Numerical Simulations on the ERICA Tiltrotor," *Aerospace Science and Technology*, Vol. 64, No. 1, 2017, pp. 171–191, doi: 10.1016/j.ast.2017.01.023.

[43] Barakos, G. N. and Johnson, C. S., "Acoustic Comparison of Propellers," *International Journal of Aeroacoustics*, Vol. 15, No. 6, 2016, pp. 575–594, doi: 10.1177/1475472X16659214.

[44] Steijl, R., Woodgate, M., and Barakos, G. N., "CFD Requirements for Efficient Smart-Rotor Analysis," *Proceedings of the 35th European Rotorcraft Forum*, ERF, Hamburg, Germany, 2009, pp. 1–11.

[45] Shu, C. W., "Essentially Non-Oscillatory and Weighted Essentially Non-Oscillatory Schemes for Hyperbolic Conservation Laws," ICASE Report 97-65, 1997.

[46] Lent, H. M., Meier, G. E. A., Muller, K. J., Obermeier, F., Schievelbush, U., and Shurmann, O., "Mechanisms of Transonic Blade-Vortex Interaction Noise," *Journal of Aircraft*, Vol. 30, No. 1, 1993, pp. 88–93, doi: 10.2514/3.10776.

[47] Beddoes, T., "Unsteady Aerodynamics Application to Helicopter Noise and Vibration Sources," Technical Report, Westland Helicopter Ltd, Yeovil, Somerset BA202YB, UK, 1990.

[48] Lewis, R. I., *Vortex Element Methods for Fluid Dynamic Analysis of Engineering Systems, Chapter 8*, Cambridge University Press, 1991.

[49] Caradonna, F., Kitaplioglu, C., McCluer, M., Baeder, J., Leishman, J. G., Berezin, C., Visintainer, J., Bridgeman, J., Burley, C., Epstein, R., Lyrintzis, A., Koutsavdis, E., Rahier, G., Delrieux, Y., Rule, J., and Bliss, D., "Methods of the Prediction of Blade-Vortex Interaction Noise," *Journal of the American Helicopter Society*, Vol. 45, No. 4, 2000, pp. 303–317, doi: 10.4050/JAHS.45.303.

[50] Hall, C. M., *High-Order Accurate Simulations of Wake and Tip Vortex Flowfield*, Ph.D. thesis, The Pennsylvania State University, USA, Dec. 1998.

[51] Lee, S. and Bershader, D., "Head-on parallel blade-vortex interaction," *AIAA Journal*, Vol. 32, No. 1, 1994, pp. 16–22, doi: 10.2514/3.11945.

[52] Morvant, R., Badcock, K., and Barakos, G., "Airfoil-Vortex Interaction Using the Compressible Vorticity Confinement Method," *AIAA Journal*, Vol. 43, No. 1, 2005, pp. 63–75, doi: 10.2514/1.5177.

[53] Cook, P. H., McDonald, M. A., and Firmin, M. C. P., "Aerofoil RAE 2822 - Pressure Distributions, and Boundary Layer and Wake Measurements," Experimental Data Base for Computer Program Assessment, AGARD Report AR 138, 1979.

[54] Tatsumi, S., Martinelli, L., and Jameson, A., "A new high resolution scheme for compressible flows past airfoil," *Proceedings of the 33rd Aerospace Sciences Meeting*, Reno, Nevada, USA, AIAA-1995-0466, 1995, pp. 1–16.

[55] Menter, F. R., "Two-Equation Eddy-Viscosity Turbulence Models for Engineering Applications," *AIAA Journal*, Vol. 32, No. 8, 1994, pp. 1598–1605, doi: 10.2514/3.12149.

[56] Biava, M., *RANS Computations of Rotor/Fuselage Unsteady Interactional Aerodynamics*, Ph.D. thesis, Dipartimento di Ingegneria Aerospaziale, Politecnico di Milano, Milano, Italy, 2007.

[57] Schultz, K.-J., Splettstoesser, W., Junker, B., Wagner, W., Schoell, E., Arnauld, G., Mercker, E., Pengel, K., and Fertis, D., "A Parametric Wind Tunnel Test on Rotorcraft Aerodynamics and Aeroacoustics (HELISHAPE) - Test Documentation and Representative Results," *Proceedings of the 22nd European Rotorcraft Forum*, ERF, Brighton, UK, 1996.

[58] Hariharan, N., Egolf, A., and Sankar, L., "Simulation of Rotor in Hover: Current State and Challenges," *Proceedings of the 52nd Aerospace Sciences Meeting*, National Harbor, Maryland, USA, AIAA-2014-0041, 2014, pp. 1–28.

[59] Hariharan, N., Egolf, A., and Sankar, R. N. L., "Helicopter Rotor Aerodynamic Modeling in Hover: AIAA Standardized Hover Evaluations," *Proceedings of the 53rd Aerospace Sciences Meeting*, Kissimmee, Florida, USA, AIAA-2015-1242, 2015, pp. 1–34.

[60] Hariharan, N., Narducci, R., Reed, E., and Egolf, T. A., "Helicopter Aerodynamic Modeling of Rotor with Tip-Shape Variations: AIAA Standardized Hover Evaluations," *Proceedings of the 54th Aerospace Sciences Meeting*, San Diego, California, USA, AIAA-2016-0031, 2016, pp. 1–42.

[61] Egolf, T. A., Hariharan, N., Narducci, R., and Reed, E., "AIAA Standardized Hover Simulation: Hover Performance Prediction Status and OUtstanding Issues," *Proceedings of the 55th Aerospace Sciences Meeting*, Grapevine, Texas, USA, AIAA-2017-1429, 2017, pp. 1–14.

[62] Baeder, J. D., Medida, S., and Kalra, T. S., "OVERTURNS Simulations of S-76 Rotor in Hover," *Proceedings of the 52nd Aerospace Sciences Meeting*, National Harbor, Maryland, USA, AIAA-2014-0045, 2014, pp. 1–11.

[63] Jain, R. K. and Potsdam, M. A., "Hover Predictions on the Sikorsky S-76 Rotor using Helios," *Proceedings of the 52nd Aerospace Sciences Meeting*, National Harbor, Maryland, USA, AIAA-2014-0207, 2014, pp. 1–22.

[64] Sheng, C., Zhao, Q., and Wang, J., "S-76 Rotor Hover Prediction using U^{2}NCLE Solver," *Proceedings of the 52nd Aerospace Sciences Meeting*, National Harbor, Maryland, USA, AIAA-2014-004, 2014, pp. 1–19.

[65] Narducci, R., "OVERFLOW Simulation of Rotors in Hover: The Boeing Company," *Proceedings of the 52nd Aerospace Sciences Meeting*, National Harbor, Maryland, USA, AIAA-2014-0208, 2014, pp. 1–9.

[66] Jimenez-Garcia, A. and Barakos, G. N., "Hover Predictions on the S-76 Rotor using HMB2," *Proceedings of the 53rd Aerospace Sciences Meeting*, Kissimmee, Florida, USA, AIAA-2015-1712, 2015, pp. 1–34.

[67] Balch, D. T. and Lombardi, J., "Experimental Study of Main Rotor Tip Geometry and Tail Rotor Interactions in Hover. Vol I - Text and Figures," NASA CR–177336, Feb. 1985.

[68] Scrase, N. and Maina, M., "The Evaluation of Propeller Aero-Acoustic Design Methods by Means of Scaled-Model Testing Employing Pressure Tapped Blades and Spinner," *Proceeding of the 19th Congress of the International Council of the Aeronautical Sciences*, Anaheim, California, USA, ICAS-94-6.1.2, 1994, pp. 183–195.

[69] Betzina, M. D., "Rotor Performance of an Isolated Full-Scale XV-15 Tiltrotor in Helicopter Mode," *Proceedings of 58th American Helicopter Society*, Montreal, Canada, AHS-58-2002-008, 2002, pp. 1–12.

[70] Felker, F. F., Betzina, M. D., and Signor, D. B., "Performance and Loads Data from a Hover Test of a Full-Scale XV-15 Rotor," NASA TM–86833, Sept. 1985.

[71] Light, J. S., "Results from an XV-15 Rotor Test in the National Full-Scale Aerodynamics Complex," *Proceedings of the 53rd American Helicopter Society Annual Forum*, AHS, Virginia Beach, Virginia, USA, 1997.

[72] Maisel, M. D., Giulianetti, D. J., and Dugan, D. C., "The History of the XV-15 Tilt Rotor Research Aircraft: From Concept to Flight," NASA SP-2000-4517, Feb. 2000.

[73] Leishman, J. G., *Principles of Helicopter Aerodynamics*, Cambridge University Press, 2006.

[74] Wadcock, A. J., Yamauchi, G. K., and Driver, D. M., "Skin Friction Measurements on a Hovering Full-Scale Tilt Rotor," *Journal American Helicopter Society*, Vol. 44, No. 4, 1999, pp. 312–319, doi: 10.4050/JAHS.44.312.

[75] Yoon, S., Pulliam, T. H., and Chaderjian, N. M., "Simulations of XV-15 Rotor Flows in Hover Using OVERFLOW," *Proceedings of the 50th AHS Aeromechanics Specialists*, AHS, San Francisco, California, USA, 2014, pp. 1–11.

[76] Bousman, W. G., "Aerodynamic Characteristics of SC1095 and SC1094R8 Airfoils," NASA TP–2003-212265, Dec. 2003.

[77] Shinoda, P. M., Yeo, H., and Norman, T. R., "Rotor Performance of a UH-60 Rotor System in the NASA Ames 80- by 120-Foot Wind Tunnel," *Proceedings of 58th American Helicopter Society*, AHS, Montreal, Canada, 2002, pp. 1–18.

[78] Dindar, M., Shephard, M. S., Flaherty, J. E., and Jansen, K., "Adaptive CFD analysis for rotorcraft aerodynamics," *Computer Methods in Applied Mechanics and Engineering*, Vol. 189, No. 1, 2000, pp. 1055–1076, doi: 10.1016/S0045-7825(99)00368-0.

[79] Kufeld, R., Balough, D., Cross, J., Studebaker, K., and Jennison, C., "Flight Testing the UH-60A Airloads Aircraft," *Proceedings of 50th American Helicopter Society*, Alexandria, Virginia, USA, AHS-50-1994-044, 1994, pp. 1–22.

[80] Jeong, J. and Hussain, F., "On the Identification of a Vortex," *Journal of Fluid Mechanics*, Vol. 285, No. 1, 2015, pp. 69–94, doi: 10.1017/S0022112095000462.

[81] "NICETRIP - Novel Innovative Competitive Effective Tilt Rotor Integrated Project: NICETRIP website," http://www.transport-research.info/project/novel-innovative-competitive-effective-tilt-rotor-integrated-project, last visited date: 14/07/2017.

[82] Alli, P., Nannoni, F., and Cicalé, M., "ERICA: The European Tiltrotor Design and Critical Technology Projects," *AIAA/ICAS, International Air and Space Symposium and Exposition: The Next 100 Years*, Day-ton, Ohio, USA, 2005.

[83] Bruin, A. and Schneider, O., "A Discussion of Measured Static and Dynamic Rotor Loads During Testing of the ERICA Tilt-Wing Rotorcraft Configuration in DNW-LLF Wind Tunnel," *Proceeding of the 40th European Rotorcraft Forum*, Southampton, UK, ERF-2014-5C, 2014, pp. 1–15.

[84] Vigevano, L., Beaumier, P., Decours, J., Khier, W., Kneisch, T., and Vitagliano, P., "Tilt-Rotor Aerodynamics Activities During the NICETRIP Project," *Proceeding of the 40th European Rotorcraft Forum*, Southampton, UK, ERF-2014-16A, 2014, pp. 1–14.

[85] Philipsen, I. and Heinrich, S., "Test Report on Measurements on the NICETRIP Large-Scale Powered Model in DNW-LLF," Project Number 2410.1338, Aug. 2013.

[86] Lebrun, F., "NICETRIP test - ERICA 1/5th Scale Powered Model in the Test Section No.2 - 45m^2 of S1MA Wind Tunnel," Test Report Number PV 1/17648 DSMA, June 2014.